

Master's thesis

Influence of Continuous Non-Abelian Symmetries on Ergodicity in Disordered Quantum Spin Chain

Dimitris Saraidaris



Faculty of Physics
Ludwig-Maximilians-Universität München

supervisors:
Prof. Dr. Jan von Delft
Dr. Andreas Weichselbaum
Jheng-Wei Li

München, 28 February 2022

Masterarbeit

Einfluß von Nicht-Abelschen Symmetrien auf Ergodizität in Ungeordneten Spin Ketten

Dimitris Saraidaris



Fakultät für Physik
Ludwig-Maximilians-Universität München

betreut von:
Prof. Dr. Jan von Delft
Dr. Andreas Weichselbaum
Jheng-Wei Li

München, 28 February 2022

Abstract

Many-Body Localization (MBL) has drawn a lot of attention, having emerged as a new phase of matter when disorder is present. Numerous studies, both theoretical and experimental, have investigated the properties of MBL and its dynamics. One goal is to understand the role of symmetry on the thermal and MBL phases. Although Abelian symmetries have been thoroughly studied, this is not the case for continuous non-Abelian symmetries. In this Master's thesis project, we study the influence of non-Abelian $SU(n)$, $n = 2, 3$ symmetries on the ergodic or non-ergodic behavior of a disordered Heisenberg quantum spin chain. While theoretical studies have proven that MBL is inconsistent with continuous non-Abelian symmetries, a recent study [1] has shown that non-ergodic behavior is still possible for an $SU(2)$ symmetric model. We will use a time-evolution tensor network method, the time-dependent density matrix renormalization group, to check some of these results, extend the analysis to larger systems, and also explore the $SU(3)$ symmetric disordered Heisenberg model.

Acknowledgements

First and foremost I would like to express my sincere gratitude to Professor Dr. Jan von Delft for giving me the opportunity to study such a fascinating topic, as well as for his constant support and numerous advice throughout my project. Working on this topic has sparked my interest in Tensor Networks and reshaped my preferences for future research goals.

I am also grateful to Dr Andreas Weichselbaum. Apart from providing the QSpace library and the tDMRG algorithm, without which this project could not have been held, his advice and countless new ideas have played a significant role to the path that this project eventually took.

I would also like to thank Jheng-Wei Li for his great help and guidance both on the theoretical and the technical part of my project. Our everyday discussions were more than fruitful and he showed great patience, especially the times when my coding mistakes were literally mind-blowing.

Special thanks to Professor Dr. Dmitry Abanin for the fruitful zoom-discussions we had and his helpful comments and feedback on my results.

Of course, I would like to express my gratitude to all the members of the Theoretical Solid State Physics group. My master project started in the middle of the pandemic (I still hope it was the middle), so my motivation was a little struck by the fact that I had to work at home. This changed when I started going to the office and finally met the members of the group in person. So, thanks to all the lunch-break members: Marcel, Björn, Nihal, Marc, Benedikt, Alex, Nick, Samira, Andreas, Héloïse, Anxiang, Nepomuk and Johannes. Special thanks to my office-mates Alex and Nick for making the office a pleasant environment.

Last but not least, I would like to thank my parents for their endless help and support, as well as my friends in Greece. Without their support, I wouldn't have started my master studies in Munich to begin with.

Ευχαριστώ

Contents

1	Thermalization vs Many-body localization	1
1.1	Thermalization in quantum systems	1
1.2	The Eigenstate Thermalization Hypothesis	2
1.3	Anderson localization	4
1.4	Definition of MBL state	5
1.5	Area law entanglement in MBL	6
1.6	Quasi-local integrals of motion	6
1.7	The thermal-MBL transition	8
1.7.1	A localization criterion	9
1.7.2	Critical value of the resonance ratio g	10
1.7.3	Scaling properties of the MBL transition	10
1.7.4	Critical dynamics	11
1.7.5	Thermalization breakdown towards MBL phase	11
1.7.6	Entanglement at the transition point	12
1.8	Example: The spin-1/2 Heisenberg chain in a random magnetic field .	12
1.8.1	Spectral statistics of ETH and MBL phases	14
1.8.2	Entanglement Entropy	14
1.8.3	Transport	15
1.8.4	Many-body mobility edge	15
1.9	Experiments	16
2	Many-body localization vs symmetry	19
2.1	Local symmetry action	19
2.2	Example of MBL phase preservation	19
2.3	Non-abelian symmetries	20
2.4	General symmetry principles	20
2.5	Systems with $SU(n)$ symmetry - what we know	21
3	Time evolution of $SU(n)$ disordered Heisenberg chains	25
3.1	$SU(2)$ symmetric model	25
3.2	$SU(2)$ - Initialization	26
3.3	$SU(3)$ symmetric model	28
3.4	$SU(3)$ - Initialization	28
3.5	Time-dependent Density Matrix Renormalization Group (tDMRG) .	29

4	Results and analysis	33
4.1	Spin-spin correlations	33
4.2	Eigenvalues of spin-spin correlations	37
4.3	Averaging over disorder	39
4.3.1	Parameters	39
4.3.2	Nearest-neighbor spin correlations $\langle \mathbf{S}_i \mathbf{S}_{i+1} \rangle$	39
4.4	Entanglement entropy scaling	42
4.5	$SU(2)$ vs $SU(3)$ symmetry	47
4.5.1	Nearest-neighbor spin correlations $\langle \mathbf{S}_i \mathbf{S}_{i+1} \rangle$	47
4.5.2	Entanglement entropy scaling	48
4.6	Dynamics of sub-thermal regime	51
5	Summary and Discussion	54
	Appendices	57
A	Tensor networks	58
A.1	Notation	58
A.2	Matrix Product States (MPS)	58
A.3	Matrix Product Operators (MPO)	59
A.4	Singular Value Decomposition (SVD)	60
A.5	Density Matrix Renormalization Group (DMRG)	60

Chapter 1

Thermalization vs Many-body localization

1.1 Thermalization in quantum systems

Let us imagine a cup of *very hot* coffee left outside in the *cold* Munich weather in January. Without any physics intuition, we can predict that, after a while, our coffee will get *cold*, or in other words, it will reach thermalization. And that is an easy prediction to make, because thermalization processes are extremely common in nature (and our everyday life).

However, describing thermalization using the modern microscopic theory, the quantum theory, is not an easy task. Although, quantum statistical mechanics can provide some accurate macroscopic predictions for some problems, difficulties arise when the models become more complicated. In order to study thermalization we picture our system weakly coupled to an environment. However, if the system-environment interactions are difficult to model, we will be led to making assumptions or even fail to describe the system. That was the case until 2008, when M. Rigol, V. Dunjko and M. Olshanii [2] proved that thermalization can be studied in isolated systems, without the need to add an environment as a thermal bath. In this case, the rest of the system acts as a bath to each subsystems.

Since then, it has been established by both theoretical studies and experiments that there exist two main classes of many-body systems: the ergodic ones and the many-body localized (MBL). In this chapter, we will review the first class of the ergodic systems and the phenomenon of thermalization in isolated quantum systems. For that, we will introduce the eigenstate thermalization hypothesis (ETH), which explains the microscopic mechanism of thermalization in isolated quantum systems [3–6].

In statistical mechanics the description of classical systems is based on the ergodicity hypothesis:

Ergodicity hypothesis (in statistical mechanics): Over a long period of time, all microstates of the system are accessed with equal probability.

In quantum systems though this description is problematic. Let us assume that

we have an isolated quantum many-body system in an initial non-equilibrium state $|\psi(0)\rangle$, such that the energy fluctuations are sub-extensive (they grow slower than the system's size). The time evolution of the initial state is determined by a Hamiltonian \hat{H} , as shown below:

$$|\psi(t)\rangle = e^{-i\hat{H}t} |\psi(0)\rangle = \sum_n A_n e^{-iE_n t} |n\rangle \quad (1.1)$$

Here, the states $|n\rangle$ are the many-body eigenstates of the system with eigenenergies E_n . Unlike a classical system, the probability $p_n = |A_n|^2$ to find a quantum system in a particular eigenstate $|n\rangle$, is determined by the initial state and does not change over time.

Let's now assume a physical observable of the system, which is described by an operator \hat{O} . The average value of operator \hat{O} after time $T \rightarrow \infty$ is given by:

$$\langle \hat{O} \rangle_\infty = \lim_{T \rightarrow \infty} \frac{1}{T} \int_0^T dt \langle \psi(t) | \hat{O} | \psi(t) \rangle \stackrel{!}{=} \sum_n p_n \langle n | \hat{O} | n \rangle \quad (1.2)$$

An isolated system, starting from an initial state, can achieve *thermalization*, if the system's observables reach values given by the microcanonical ensembles at sufficient long times. Thus, the expectation values in individual eigenstates, $\langle n | \hat{O} | n \rangle$, need to follow the microcanonical ensemble, in order for the observable \hat{O} to reach a thermal expectation value for $T \rightarrow \infty$, since p_n are fixed.

1.2 The Eigenstate Thermalization Hypothesis

The question we want to answer now is: *Why ergodic systems thermalize?* J.M. Deutsch [3] (1991) and M. Srednicki [4] (1994) proposed the Eigenstate Thermalization Hypothesis (ETH), as an explanation of the thermalization phenomenon using the properties of individual eigenstates. In particular, the ETH states that, in ergodic systems, the expectation values in individual states, $\langle n | \hat{O} | n \rangle$, follow the microcanonical ensemble. It is important to mention here, that although all known examples of thermalizing systems obey ETH, it is not clear yet if ETH is a necessary condition for thermalization.

In Eq.1.1, we have assumed that the off-diagonal terms $\langle \alpha | \hat{O} | \beta \rangle$ average out. However, in order to describe the approach to the equilibrium values and bound the temporal fluctuations around a certain energy, we also need to take the off-diagonal terms under consideration. In that case, the Eigenstate Thermalization Hypothesis ansatz [7] is introduced:

$$\langle \alpha | \hat{O} | \beta \rangle = \mathcal{O}_{mc}(\bar{E}) \delta_{\alpha\beta} + e^{-S_{th}^{\bar{E}}/2} R_{\alpha\beta} f(\omega, \bar{E}) \quad (1.3)$$

where $\bar{E} = (E_\alpha + E_\beta)/2$ denotes the average eigenenergy and $\omega = E_\alpha - E_\beta$ the energy difference. $S_{th}^{\bar{E}}$ is the thermodynamic entropy, $R_{\alpha\beta}$ is a normal-distributed random number, \mathcal{O}_{mc} the microcanonical expectation value of local observable and $f(\omega, \bar{E})$ is the spectral function. It is important for functions $\mathcal{O}_{mc}(\bar{E})$ and $f(\omega, \bar{E})$ to be smooth functions of their arguments. The ansatz above is sufficient to ensure thermalization.

In order to understand why the above ansatz makes sense intuitively, we will discuss the diagonal and off-diagonal terms separately.

- diagonal term

As we saw in Eq.1.2, the infinite time mean value of an observable can be written as:

$$O_\infty = \lim_{T \rightarrow \infty} \frac{1}{T} \int_0^T dt \sum_{m,n} c_m^* c_n O_{mn} e^{i(E_n - E_m)t} = \sum_n |c_n|^2 O_{nn} \quad (1.4)$$

as the time integral kills all the terms with $E_m \neq E_n$. This implies that the diagonal matrix elements must be given by the microcanonical value for each eigenstate. That is why function $\mathcal{O}_{mc}(\bar{E})$ has to be a smooth function of energy, which is equivalent to the microcanonical value. The diagonal term of the ETH ansatz contains exactly this information.

- off-diagonal term

Let's consider temporal fluctuations of the observable O .

$$\begin{aligned} \sigma_O^2 &= \lim_{T \rightarrow \infty} \frac{1}{T} \int_0^T dt (\langle O(t) \rangle^2 - O_\infty^2) = \\ &= \lim_{T \rightarrow \infty} \int dt \sum_{m,n,p,q} O_{mn} O_{pq} c_m^* c_n c_p^* c_q e^{i(E_n - E_m + E_p - E_q)t} - O_\infty^2 \end{aligned} \quad (1.5)$$

The term that contributes is the one for $E_n = E_q$ and $E_m = E_p$, which gives:

$$\sigma_O^2 = \sum_{m \neq n} |c_m|^2 |c_n|^2 |O_{mn}|^2 \leq \max |O_{mn}|^2 \quad (1.6)$$

for the off-diagonal elements. $f(\omega, \bar{E})$ function determines the dynamics of the observable. One way to see that is to calculate the correlation function $\langle m | \hat{O}(t) \hat{O}(0) | n \rangle$ using the ETH ansatz, as follows:

$$\langle m | \hat{O}(t) \hat{O}(0) | n \rangle = \int e^{i\omega t} |f_O(\bar{E}, \omega)|^2 d\omega \quad (1.7)$$

where the absorption rate is $A(\omega) = |f_O(\bar{E}, \omega)|^2$.

ETH provides also an insight to the entanglement properties of ergodic eigenstates. Assuming that the eigenstate $|n\rangle$ obeys ETH, then a small subsystem A will have thermal expectation values. Therefore, the entanglement entropy of subsystem A in state $|n\rangle$ is equal to the thermodynamic entropy, as follows:

$$S_{ent}(A) = -Tr(\rho_A \log \rho_A) = S_{th}(A) \quad (1.8)$$

Since thermodynamic entropy is extensive, this implies that for highly excited eigenstates $|n\rangle$ the entanglement entropy obeys the volume law, scaling proportionally to the volume of the subsystem, $S_{ent}(A) \propto \text{vol}(A)$.

The ansatz Eq.1.3 also implies the strong sensitivity of ergodic eigenstates to external perturbations of the Hamiltonian, from which it follows that there is level repulsion. Indeed, if we add a small perturbation, $\epsilon\hat{O}$, $\epsilon \ll 1$, to the Hamiltonian, the off-diagonal elements Eq.1.6 are exponentially larger than the level spacing $\Delta \sim D e^{-S_{th}^E/2}$, where D is the characteristic energy scale of the Hamiltonian. Thus, the effect of a local perturbation is not local, but it effects an exponentially large number of eigenstates. The level spacing, then, obeys Wigner-Dyson statistics, where the eigenenergies behave as independent random variables and level repulsion is present.

How to escape thermalization

In order for a system to reach thermalization, transport must be present. In particular, the different ergodic subsystems are required to exchange energy and particles, meaning that the system must be conducting. Therefore, it is reasonable to assume that the absence of transport could be a way to escape thermalization. The starting point could be the Anderson localization in single-particle disordered systems.

1.3 Anderson localization

The first introduction of the localization of quantum particles by a static random potential was introduced by P.W. Anderson in his seminal paper "Absence of Diffusion in Certain Random Lattices" [8]. It is important to note here, that this study considers localization of a single particle, while MBL theory studies many-body systems of interacting particles at finite temperature, as we will see later.

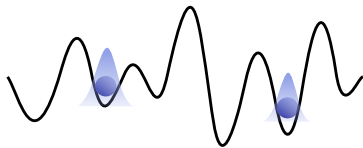


Figure 1.1: Due to strong disorder, the probability of a particle to make a resonant transition vanishes

Anderson considered a tight-binding model of electrons on a crystal lattice, where the energy levels at each site are chosen by a random distribution. The Hamiltonian of the system is given by:

$$H = \sum_i \epsilon_i c_i^\dagger c_j + \sum_{\langle i,j \rangle} t_{ij} \epsilon c_i^\dagger c_i \quad (1.9)$$

where the energies of each site are chosen randomly from a distribution with $\epsilon_i \in [-W, W]$. This is where disorder appears to the problem.

The phenomenon of Anderson localization implies that the eigenstates are localized around a center site. We can write the wavefunction as follows:

$$\Psi(r) \sim e^{-\frac{r-r_0}{\xi}} \quad (1.10)$$

where r_0 is the position of the center around which the eigenstate is localized and ξ is the localization length.

Let us now consider the limit of strong disorder, $t \ll W$. We will work with just two sites with hopping amplitude t between them.

The Hamiltonian for these two sites will be:

$$H_{1,2} = \begin{bmatrix} \epsilon_1 & t \\ t & \epsilon_2 \end{bmatrix} \quad (1.11)$$

Within first order perturbation theory we can find that:

$$|\Psi_1\rangle \simeq |1\rangle + \frac{t}{\epsilon_1 - \epsilon_2} |2\rangle \quad (1.12)$$

and

$$|\Psi_2\rangle \simeq |2\rangle - \frac{t}{\epsilon_1 - \epsilon_2} |1\rangle \quad (1.13)$$

The above result stands in the case that the two nearby sites are off resonant. However, considering that the energy for each site is randomly distributed, the case of two sites being resonant $|\epsilon_1 - \epsilon_2| \leq t$ is possible. In particular there a finite small density of resonant pair of sites.

However, these unusual resonant sites will be in general spatially far apart, so that their overlap is exponentially small. Therefore, the question that appears here is, whether the system could be delocalized due to higher order processes. By calculating higher order perturbations, Anderson proved that, since there are intermediate non-resonant processes between the two remote resonant sites (assuming that the typical distance between them is $l \sim N^{1/d}$, where N is the number of levels and d the spacial dimension), the amplitude between them decays exponentially with l , while the level spacing only decays as a power law with l ($\delta \sim W/N$). Therefore, the long range processes do not lead to de-localization of the system.

1.4 Definition of MBL state

Now, it is time to move from the single-particle localization to the many-particle localization. We define a many-body localized (MBL) system as the system, which can be described by a complete set of conserved quantities $\{n_\alpha\}$ with $\alpha = 1, \dots, N$, each of which takes values from a set $\{1, \dots, d_\alpha\}$, and their associated quasi-local conserved projectors called 1-bits:

$$\Pi_\alpha^{n_\alpha} = \sum_{n_\beta \neq \alpha=1}^{d_\beta} |n_1 \dots n_\alpha \dots n_N\rangle \langle n_1 \dots n_\alpha \dots n_N| \quad (1.14)$$

which are exponentially well-localized within a localization length ξ of position r_α and commute with the Hamiltonian, $[\Pi_\alpha^{n_\alpha}, H] = 0$. The quasi-local conserved quantities are related to local operators after a quasi-local unitary transformation.

The known phenomenology of MBL systems, such as area-law entanglement, absence of transport, slow dephasing and entanglement growth can be based on the above definition.

1.5 Area law entanglement in MBL

As mentioned above, for systems that obey ETH the entanglement entropy of a subsystem A obeys the volume law, $S_{ent}(A) \propto \text{vol}(A)$. On the contrary, a subsystem A in an MBL eigenstate obeys the area-law, $S_{ent}(A) \propto \text{vol}(\partial A)$, meaning that it scales proportional to the volume of the boundary of the subsystem A. In fact, even highly excited MBL states obey the area-law.

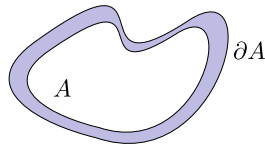


Figure 1.2: Area-law of entanglement entropy, only the boundary contributes to the entanglement

Let us now consider an MBL system with a local Hamiltonian \hat{H} . We can divide the Hamiltonian into: \hat{H}_A , which acts on a subsystem A, \hat{H}_B , which acts on the complement subsystem of A, B, and V_{AB} which couples the subsystems A and B locally near the boundary. Starting in the limit $V_{AB} \rightarrow 0$, the eigenstates can be written as a tensor product of the eigenstates $|\alpha\rangle_A, |\beta\rangle_B$ of \hat{H}_A and \hat{H}_B :

$$|AB\rangle = |\alpha\rangle_A \otimes |\beta\rangle_B \quad (1.15)$$

The subsystem A has zero entanglement entropy. Now we turn on the local coupling term V_{AB} , which can be interpreted as a local perturbation of the MBL state, affecting the subsystems within a localization length ξ from the boundary of A and B. A local perturbation far away of the boundary is expected to decay exponentially with the distance, leading to an area-law scaling of the entanglement entropy $S_{ent} \propto \text{vol}(\partial A)$.

1.6 Quasi-local integrals of motion

We will try now to understand the definition in section 1.4 in more detail. We consider the disordered Heisenberg model:

$$\hat{H}_{XXZ} = \frac{J_\perp}{2} \sum_{i=1}^L (\hat{\sigma}_i^x \hat{\sigma}_{i+1}^x + \hat{\sigma}_i^y \hat{\sigma}_{i+1}^y) + \frac{J_z}{2} \sum_{i=1}^L \hat{\sigma}_i^z \hat{\sigma}_{i+1}^z + h_i^z \hat{\sigma}_i^z \quad (1.16)$$

where $\hat{\sigma} = (\hat{\sigma}^x, \hat{\sigma}^y, \hat{\sigma}^z)$ is the vector of the spin-1/2 Pauli operators and $h_i^z \in [-W, W]$ is a randomly distributed on-site magnetic field and W is the disorder strength.

We start by taking the limit $J_{\perp} \rightarrow 0$ of the XXZ-Hamiltonian:

$$\hat{H}_0 = J_z \sum_{i=1}^L \hat{\sigma}_i^z \hat{\sigma}_{i+1}^z + \sum_i h_i^z \hat{\sigma}_i^z \quad (1.17)$$

The Hamiltonian \hat{H}_0 commutes with each operator $\hat{\sigma}_i^z$, $[\hat{H}_0, \hat{\sigma}_i^z] = 0$, therefore there are 2^N eigenstates, which are product states of the form:

$$|\{\sigma\}\rangle = |\sigma_1 \sigma_2 \dots \sigma_N\rangle \quad (1.18)$$

where $\sigma_i = \uparrow, \downarrow$

The system at this point is in the Many-body localization (MBL) state, for $W \neq 0$. Now, we turn on a weak J_{\perp} term ($J_{\perp} \ll W$), such that the system remains in the MBL state, but the Hamiltonian is no longer diagonal in the $|\{\sigma\}\rangle$ basis. Using the same argument we used for the entanglement entropy above, we can claim that the new eigenstates can be obtained from the product state, Eq.1.18, by a quasi-local unitary transformation \hat{U} [9–11].

Quasi local operator \hat{U} : The operator is defined as quasi-local, if it can be factored into a sequence of 2-site, 3-site,... unitary operators as $\hat{U} = \prod_i \dots \hat{U}_{i,i+1,i+2}^{(3)} \hat{U}_{i,i+1}^{(2)}$ (Fig.1.3).

Therefore, we obtain the integrals of motion $\hat{\tau}_i^z$ of \hat{H} from the integrals of motion $\hat{\sigma}_i^z$ by the unitary transformation:

$$\hat{\tau}_i^z = \hat{U}^\dagger \hat{\sigma}_i^z \hat{U} \quad (1.19)$$

At stronger disorder we can write $\hat{\tau}_i^z$ as an expansion of $\hat{\sigma}_i^z$, as follows:

$$\hat{\tau}_i^z = Z \hat{\sigma}_i^z + \sum_{n=1}^{\infty} V_i^{(n)} \hat{O}_i^{(n)} \quad (1.20)$$

where $\hat{O}_i^{(n)}$ contains up to $(2n+1)$ -body operators acting on sites at distance n from site i and is normalized to $\|\hat{O}_i^{(n)}\| = 1$. Z is the finite overlap of $\hat{\tau}_i^z$ with $\hat{\sigma}_i^z$ and the coefficients $V_i^{(n)} \sim e^{-n/\xi}$, satisfies the constraint that the $\hat{\tau}_i^z$ act on spins locally. The lengthscale ξ can be viewed as the *localization length* of the MBL phase, and the existence of this locality distinguishes the MBL phase from the thermal phase.

The operators $\hat{\tau}_i^z$ form a complete set of independent quasi-local integrals of motion (LIOMs) and can be viewed as an emergent conserved pseudospin degree of freedom, as it is conserved during the evolution of the MBL system, as long as it is not coupled to an external heat bath. We can also define the operators $\hat{\tau}_i^{x,y} = \hat{U}^\dagger \hat{\sigma}_i^{x,y} \hat{U}$, which form a complete basis together with $\hat{\tau}_i^z$, so that the operators $\hat{\sigma}_i^\alpha$ can be decomposed in the τ -basis.

In order to study the dynamics of the system, described by the Hamiltonian \hat{H} , in the MBL phase, it is useful to write it in the τ -basis, as follows:

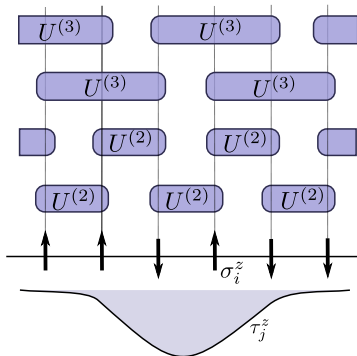


Figure 1.3: Quasi-local operator \hat{U} , written as a sequence of 2-site and 3-site unitary operators

$$\hat{H}_{MBL} = \sum_i h_i \hat{\tau}_i^z + \sum_{i>j} J_{ij} \hat{\tau}_i^z \hat{\tau}_j^z + \sum_{i<j<k} J_{ijk} \hat{\tau}_i^z \hat{\tau}_j^z \hat{\tau}_k^z + \dots \quad (1.21)$$

We note that the above Hamiltonian has a very simple form, including only $\hat{\tau}_i^z$ terms, which is reasonable as $[\hat{\tau}_i^z, \hat{H}] = 0$. The coupling constants decay exponentially with the separation between the LIOMs, as:

$$J_{ij} \propto J_0 e^{-|i-j|/\kappa} \quad (1.22)$$

and

$$J_{ijk} \propto J_0 e^{-|i-k|/\kappa} \quad (1.23)$$

By equating the Hamiltonian \hat{H}_{MBL} to the original \hat{H} we can derive an equality that connects the lengthscales κ and ξ :

$$\kappa^{-1} \geq (\xi^{-1} + \ln 2)/2 \quad (1.24)$$

The above expression indicates κ remains finite, even if ξ diverges at the MBL-thermal transition.

1.7 The thermal-MBL transition

In this section, we will discuss about the transition between the thermal and MBL phases. These two phases are characterized by quite different dynamical properties, therefore they must be separated by a phase transition[12–14]. While crossing the transition point, there is a drastic change of the entanglement structure from volume- to area-law. Such many-body localization (delocalization) transitions bear few similarities with the familiar paradigms of fully-thermal and fully quantum phase transitions, so understanding this new kind of criticality is of great significance.

1.7.1 A localization criterion

Here, we introduce a rough criterion[12], that will enable us to determine if a state lives in the thermal or MBL phase, with a later goal to understand the transition between them. For that we will again consider the 1-D spin chain system with Hamiltonian:

$$\hat{H}_0 = \sum_{i=1}^L J \hat{S}_i \hat{S}_{i+1} + \sum_i h_i \hat{S}_i^z \quad (1.25)$$

where $h_i \in [-W, W]$ is randomly distributed and represents the disorder.

To test localization, we will start by computing the transition amplitude Γ , for our system from an initial product state $|\Psi\rangle$ to a final state $|\Psi'\rangle$. For a transition between two typical infinite-temperature spin configurations, we need to flip $\sim O(L)$ spins, leading to a total transition amplitude of:

$$\Gamma \simeq \left(\frac{W}{J}\right)^L \simeq e^{-L/x_0} \quad (1.26)$$

where $x_0 \simeq (\log W/J)^{-1}$ is the single particle localization length. For weak disorder, the transition amplitude gives an asymptotic form $\Gamma \sim 2^{-L/2}$, as in the thermal phase eigenstates are random superpositions of all typical spin configurations.

In order to check whether such a typical macroscopic rearrangement of spins occur resonantly, we will compare the transition amplitude with the energy level spacing δ between the states. In our case the energy level spacing is given by:

$$\delta \simeq \frac{\Lambda}{2^L} \simeq \frac{\sqrt{L}}{2^L} \quad (1.27)$$

where $\Lambda \sim \sqrt{L}$ is the many-body bandwidth. We introduce the dimensionless ratio g , as:

$$g = \Gamma/\delta \quad (1.28)$$

which measures the degree to which transitions between different spin configurations are resonant.

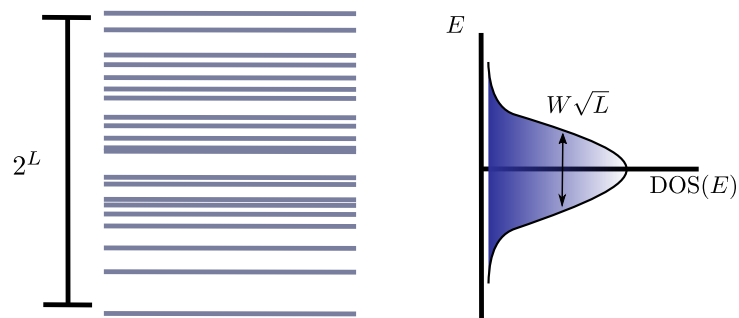


Figure 1.4: The many body level spacing as a criterion to distinguish between thermal and MBL phase

In particular, for strong disorder, meaning $g \ll 1$ the eigenstates are perturbatively close to non-entangled product states, with limited many-body tunneling processes, which represent the MBL-like picture. On the other hand, $g \gg 1$ means that resonant tunneling between all typical spin configurations is present, a picture consistent with the thermal phase.

1.7.2 Critical value of the resonance ratio g

As mentioned above, the thermal-MBL transition has unique characteristics. The resonance ratio g is a random, fluctuating function of the disorder, where the fluctuations are extremely strong. As a result, it would be wrong to assume that the transition occurs when $g_c \simeq 1$. As the parameter g characterizes collective many-body resonances, it is exponentially sensitive to extensive fluctuations. This leads to the fact that the mean value of g is ill-defined, and we must study its full distribution instead. Thus, the MBL transition can be viewed as a strong-randomness phase transition.

One way to study the transition for our system, keeping in mind that g is characterized by strong randomness, is to separate our system into blocks of thermal regions ($g \ll 1$) and blocks of insulating ones ($g \gg 1$). The tricky case of $g \sim 1$ is not likely to appear, given the broad distribution of g , something that makes the problem easier to deal with.

Now the question that arises is: how big do the thermal or insulating blocks need to be for the system to be in the thermal or MBL phase respectively? Let us assume two locally thermal clusters of length l separated by a locally insulating cluster of length $L - 2l$ (Fig.1.5). The two thermal clusters can interact via tunneling through the MBL block with amplitude $\sim e^{-(L-2l)/x_0}$, where x_0 is the localization length. For an adequately large interaction (larger than the level spacing $\delta \sim 2^{-2l}$) the two thermal cluster will inter-resonate and form a big thermal cluster, for $l = l_* \simeq \frac{L}{2(1+x_0/\log 2)}$. Therefore for $l > l_*$, the thermal blocks act as a bath, that thermalizes the intermediate localized spins. The transition is expected for thermal block sizes close to l_* .

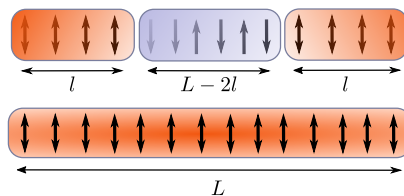


Figure 1.5: Locally thermal and insulating clusters

1.7.3 Scaling properties of the MBL transition

Upon weakening the disorder, an 1-dimensional MBL system melts directly into an incoherent thermal liquid via a continuous second order phase transition. Studies

have shown that this phase transition is governed by a diverging length scale:

$$\xi \sim \frac{1}{|\Delta W|^\nu} \quad (1.29)$$

where $\Delta W = W - W_c$, with W_c being the critical value of the disorder and ν is the correlation length exponent. Exact diagonalization simulations have found $\nu_{ED} \simeq 1$, while RG approaches suggest larger values like $\nu_{RG} \simeq 3.2 - 3.5$ [15, 16].

1.7.4 Critical dynamics

As we argued above, the critical point of the transition between the two phases is determined by locally thermal blocks tunneling through MBL blocks, that fill the system. The characteristic time that is needed to tunnel through an MBL block of length $\sim L$, therefore thermalize the localized spins, is exponentially slow at the transition point:

$$\tau(L)|_{W=W_c} \sim e^{-L} \quad (1.30)$$

We can compare this with characteristic times of ordinary critical points, where $\tau \sim L^z$, with z is a finite dynamical exponent and conclude that critically (de-)localized systems have dynamics with infinite dynamical exponent $z \rightarrow \infty$.

MBL systems do not reach equilibrium, they have virtual dephasing dynamics and strictly zero long-distance transport of conserved quantities, like energy or particles. In contrast, for $L \ll \xi$ an exponentially slow non-zero transport is present, driving the system to equilibrium.

1.7.5 Thermalization breakdown towards MBL phase

Next, we will discuss about how the transport and relaxation dynamics slowly stop at the MBL transition. Starting from the thermal side, where we expect $\tau(L) \sim DL^2$ (D is the diffusion constant), we want to approach the transition on scales $L \ll \xi$. RG approaches, as well as exact diagonalization simulations have found that near the transition the relaxation is never diffusive, but scales like $\tau(L) \sim L^z$ with $z > 2$. The dynamical exponent z continuously evolves in respect to the disorder at a diverging way, as:

$$z_{\mathcal{O}} = \frac{c_{\mathcal{O}}}{|W - W_c|^\nu} \quad (1.31)$$

where $c_{\mathcal{O}}$ is a non-universal number that depends on the observable \mathcal{O} that is relaxing to equilibrium. These observables \mathcal{O} , which can be the energy or entanglement for example, have different dynamical critical exponents, but diverge with the same universal power law in the vicinity of the transition point.

These unusual sub-diffusive dynamics can be explained by the existence of rare insulating regions between the thermal regions, which slow down relaxation and transport. Let us assume that there is such an insulating region of length r within a wide thermal region. On the thermal side of the transition the probability of finding such

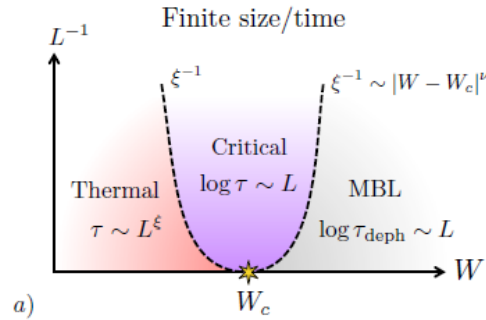


Figure 1.6: **Plot taken from [12]:** Scaling structure of the MBL transition

an insulating region scales as $e^{-r/\xi}$, where ξ is the correlation length. The characteristic relaxation time of this region scales as $\tau(r) \sim e^{r/x_0}$, which means that the expected time diverges near the transition, where $\xi > x_0$.

The size of these bottleneck-type regions scales as:

$$r_* \sim \xi \log L / \xi \quad (1.32)$$

and the relevant tunneling time scales as:

$$\tau(r_*) \sim e^{r_*/x_0} \sim L^{\xi/x_0} \quad (1.33)$$

This is in accordance with Eq.1.31, as the correlation length diverges as $\xi \sim 1/|W - W_c|^\nu$.

1.7.6 Entanglement at the transition point

Entanglement plays a key role to the study of the thermal-MBL transition, as well as MBL phase in general, and its behavior is addressed in most of the studies on that topic. However, there is not a clear picture concerning the scaling of entanglement right at the transition so far. For small subsystems, $L_A \ll L$, and assuming that the entropy is a continuous scaling function of L_A/ξ , it is proven that the entanglement entropy follows a thermal volume-law scaling at the MBL criticality. However, exact diagonalisation studies [17–19], on cases that are not in the small subsystem regime, have found a sub-thermal regime, as well as a discontinuity of the entanglement entropy at the transition point. For cases where $L \gg \xi$, with ξ being the characteristic length scale, entanglement entropy displays a discontinuity across the transition, from a thermal volume-law to an area-law.

1.8 Example: The spin-1/2 Heisenberg chain in a random magnetic field

Now we will study the example of a spin-1/2 Heisenberg chain in a random magnetic field to understand the properties of both thermal and MBL phases, discussed above. This example is the most studied one [20], thus perfect for this goal.

The Hamiltonian of this one-dimensional lattice model is given by:

$$\hat{H} = J \sum_{i=1}^L (\hat{\sigma}_i^x \hat{\sigma}_{i+1}^x + \hat{\sigma}_i^y \hat{\sigma}_{i+1}^y + \hat{\sigma}_i^z \hat{\sigma}_{i+1}^z) + h_i^z \hat{\sigma}_i^z \quad (1.34)$$

where the magnetic fields h_i are randomly distributed with a disorder strength $h_i \in [-W, W]$. The symmetry of the model is $U(1)$ as the total magnetization is conserved.

Using this example we will discuss about both thermal (ETH) states and MBL states especially for models that describe:

- isolated quantum systems
- eigenstates at finite energy density (far from the ground state)
- lattice systems with energy spectrum that is often bounded
- one-dimensional systems with short-range interactions

Thermalization phase

For sufficiently low disorder the system satisfies the eigenstate thermalization hypothesis (ETH), with the assumptions about the diagonal and off-diagonal elements of ETH ansatz we mentioned in the previous chapter. These assumptions have been verified numerically in a variety of studies on different systems [2, 21, 22]. We expect to verify the ETH for energies close to the middle of the spectrum, as for the spectrum extrema, convergence to ETH expectations is slower. This is the reason why Fig.1.7 includes data in the range $\epsilon \in [0.15, 0.9]$.

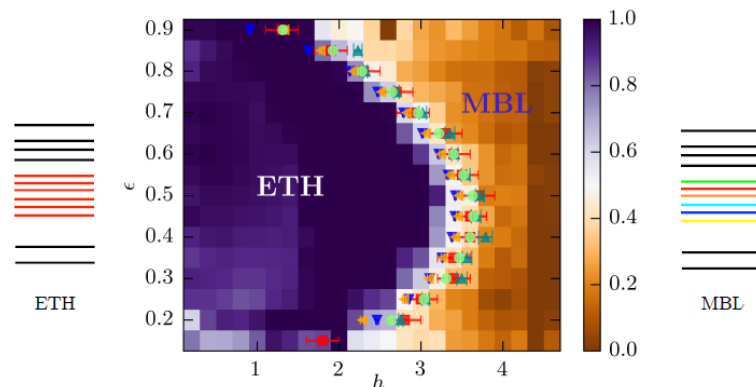


Figure 1.7: **plot taken from [17]**: Phase diagram of the random field Heisenberg spin chain, where the vertical axis is the normalized energy density and horizontal axis is the disorder strength h

Thermal eigenstates that live at the same energy density (same ϵ) have the same expectation value for few-body observables, therefore can be considered similar. in Fig.1.7 these states are depicted with the same color. Especially in the middle of the spectrum, which corresponds to infinite temperature, eigenstates behave exactly like

random vectors, and can be described by statistical mechanics.

Many-body localization (MBL) phase

In order to avoid the ETH picture, and as a consequence thermalization, sufficiently strong disorder is necessary. For our example Hamiltonian, in the strong disorder limit $h \rightarrow \infty$, the eigenstates become product states of the form $|\{\sigma\}\rangle = |\sigma_1\sigma_2\dots\sigma_N\rangle$, with $\sigma_i^z = \pm 1$. These eigenstates do not satisfy the ETH and the system does not end up in the thermal phase. Instead it is localized and without any interaction there is no particular mechanism, which could lead to energy or particle exchange. Nevertheless, the MBL phase can be present even for systems with interactions between particles in the presence of disorder [23, 24].

1.8.1 Spectral statistics of ETH and MBL phases

Here we will discuss the different properties of the eigenstates that are connected with the existence of an ETH or MBL state.

Firstly, let us discuss the spectral statistics of the two phases. In the ETH phase, the eigenvalues follow the statistics of Random Matrix Theory. For the model Eq.1.34, the eigenvalues follow the Gaussian Orthogonal Ensemble (GOE) statistics, as the Hamiltonian has only real elements in the σ^z basis. As a result the eigenvalues satisfy the Wigner semi-circle law and the level spacings $s_n = E_n - E_{n-1}$ distribution the Wigner-Dyson law.

One way to distinguish ETH from MBL phase is to compute the average ratio of consecutive level spacings $r_n = \frac{\min(s_n, s_{n-1})}{\max(s_n, s_{n-1})}$, as introduced by Oganesyan and Huse[25]. In the GOE ensemble, for the case of the ETH phase, the average value is $\langle r \rangle_{GOE} \simeq 0.5307$, while in the MBL phase, where eigenvalues are not correlated and thus follow the Poisson distribution, it takes the value $\langle r \rangle_{Poisson} \simeq 2 \ln(2) - 1 \simeq 0.386$.

A second way to distinguish the two phases is by studying the eigenstates. The eigenstates of a system that satisfies the ETH are similar, while for a MBL system they are different. Therefore, we can compare the distribution of amplitudes, $p_i = |\langle n|i \rangle|^2$, of two nearby eigenstates, with respect to the basis state $|i\rangle$, with the Kullback Leibler divergence: $KL = -\sum_i p_i \ln \frac{p_i}{p'_i}$. If the system satisfies the ETH, then the GOE ensemble will give $\langle KL \rangle_{GOE} = 2$, while if the system is in the MBL phase, $\langle KL \rangle$ diverges with respect to the system size.

1.8.2 Entanglement Entropy

In the MBL phase entanglement entropy follows the area law, especially $S_A = O(1)$ for a spin chain. Exact diagonalization results for the chain system of our example are shown in Figure 1.8. In particular, the disorder average entanglement entropy of half chains $L_A = L/2$ for an excited state of high energy ($\epsilon = 0.5$) is shown as a function of the size of the system L and disorder strength h . At disorder strength $h \simeq 3.8$ the entanglement entropy moves from the volume- to area-law. We can make the following observations about MBL states concerning entanglement properties:

- MBL states at finite energy are related to ground states of many body systems that satisfy the area-law

- MBL states can be represented by matrix product states (MPS)

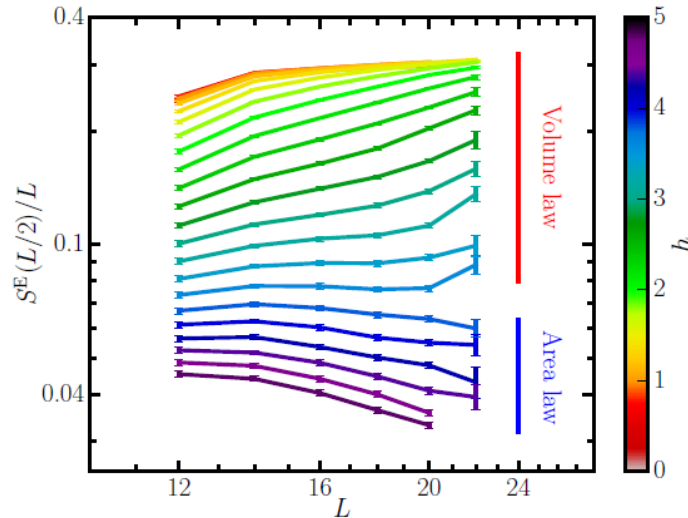


Figure 1.8: **plot taken from [17]**: Exact diagonalization results of the entanglement entropy for the random filed Heisenberg model

1.8.3 Transport

Thermalization in states that satisfy the ETH is the result of transport of energy, particles and information. In the case of MBL states transport is absent. There are studies [26, 27], where numerical calculations of the conductivity are made for our example model in Eq.1.34. In the MBL phase, the dc conductivity $\sigma_{dc} = \lim_{\omega \rightarrow 0} \sigma(\omega)$, was found to vanish for any finite temperature. However, for very low disorder, where the states satisfy the ETH, it is very difficult to numerically prove that the system has a metallic behavior.

1.8.4 Many-body mobility edge

A debated topic concerning ETH and MBL states is whether the location of the transition line between the two phases depends on the energy density. As we can see in Fig.1.7, the transition line clearly depends on the energy density. This is so-called many-body mobility edge. There are plenty of studies of the same or other models that have found a mobility edge [28–32].

However, there are studies [33] which argue that no many-body mobility edge can exist in the thermalization limit. This claim is based on the argument that local mobile fluctuations are always possible. This fluctuations have higher energy than the background and can thermalize the “cold” subsystems, leading to thermalization.

1.9 Experiments

Searching for MBL in experiments is a quite challenging task. The reason is that the systems have to remain disconnected from any thermal bath, which is difficult to achieve during experimental processes. Thus, most of the efforts done so far include ultracold atoms experiments, ultracold ions experiments, superconducting qubits experiments and a few attempts with real materials[34].

The first experiments concerning MBL[35] were based on ultracold atoms at high energy densities. The authors studied the one-dimensional Fermi Hubbard chain of interacting spin mixtures of two spin components. In the presence of a quasiperiodic potential the Hamiltonian takes the form:

$$\hat{H} = -J \sum_{i,\sigma} (\hat{c}_{i,\sigma}^\dagger \hat{c}_{i+1,\sigma} + \text{h.c.}) + \Delta \sum_{i,\sigma} \cos(2\pi\beta i + \phi) \hat{n}_{i,\sigma} + U \sum_i \hat{n}_{i,\uparrow} \hat{n}_{i,\downarrow} \quad (1.35)$$

where $\hat{c}_{i,\sigma}^{(\dagger)}$ are the fermionic operators, U is the onsite interaction strength and Δ the strength of the quasiperiodic detuning potential. The initial state prepared, was a density-wave state where particles occupy even sites. Then, the imbalanced $I = \langle (N_e - N_o)/(N_e + N_o) \rangle$ was measured for different potential strengths. What was observed (Fig.1.9), is that for weak detuning potential the imbalance relaxed rapidly, while for stronger detuning potential it saturates to a non-zero value. The first case indicates thermalization, while the second case is clear evidence of localization.

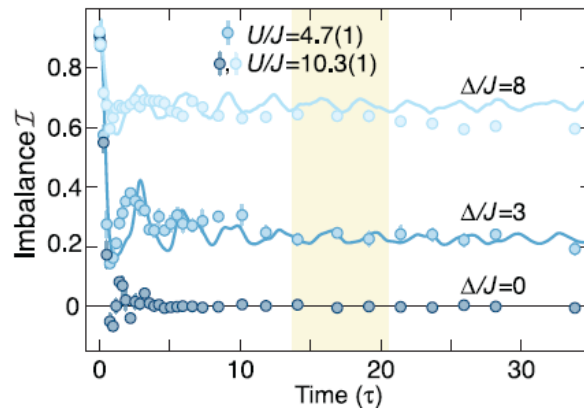


Figure 1.9: **plot taken from [35]**: Time evolution of initial density wave in a quasiperiodic potential in the interacting Aubry-André model. The plot shows the imbalance for different detuning potential strengths, providing evidence of non-ergodicity

Moreover, an experiment [36] in a two-dimensional system of interacting bosons in presence of a two dimensional disorder pattern showed evidence of localization for strong disorder (Fig.1.10).

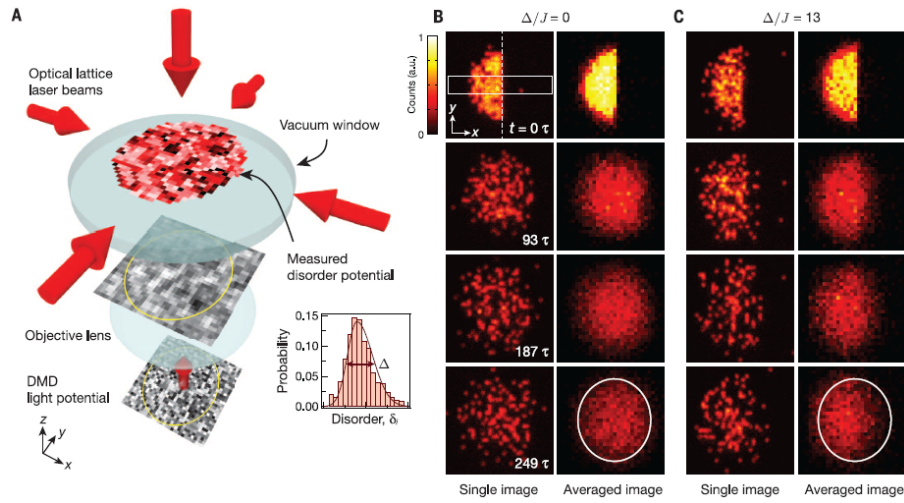


Figure 1.10: **plot taken from [36]** Evidence of non-ergodicity in two dimensions. Starting with a domain wall of a bosonic Mott insulator, time evolutions shows that the domain wall does not fully disappear after long time

Evidence of a localized phase were also presented in an experiment with ultracold ions[37]. In particular, the disordered transverse field Ising model with long range interactions was simulated by ten ultracold ions. The authors observed that starting from an initial Néel state, a stationary magnetization appeared for a strong disorder.

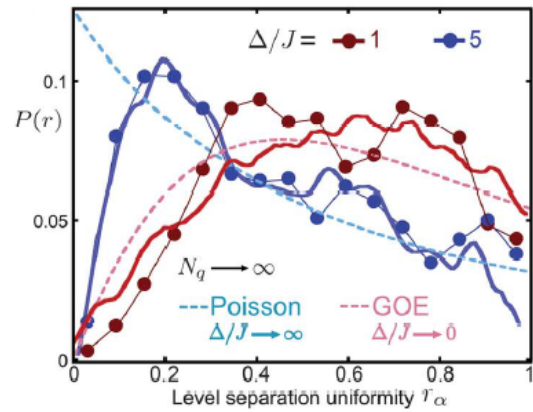
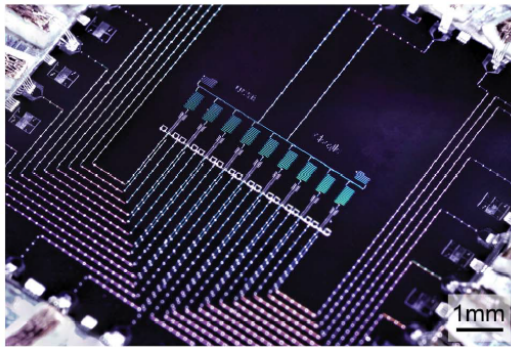


Figure 1.11: **taken from [38]** Left panel: Optical micrograph of the superconducting qubits device used for the experiment. Right panel: For a system of two interacting photons on nine lattice sites and a local disorder potential, the level spacing statistics changes from a Gaussian orthogonal ensemble for weak disorder to a Poisson distribution for weak disorder

Finally, superconducting qubit circuits[39] have been used in search for localization. The MBL level statistics have been studied[38] for disordered and non-disordered systems, revealing different behavior for each case Fig.1.11. In a different experiment[40], the disordered XY-spin Hamiltonian was simulated by ten superconducting qubits, showing again evidence of a localized phase.

Chapter 2

Many-body localization vs symmetry

One of the many directions that MBL studies take, try to find answers on how symmetry affects whether the system has MBL or thermal tendencies. In this section we will discuss about some general constraints that are imposed on many-body localization in the presence of symmetry. This chapter contains all the knowledge we had before this master project.

2.1 Local symmetry action

Let us consider a lattice of N sites. The degrees of freedom of the system transform under a faithful representation \mathcal{V} of a symmetry group G . The Hilbert space of the system of N -site lattice can be written as a tensor product of on-site Hilbert spaces, as $\mathcal{H} = \mathcal{V}^{\otimes N}$. As we have considered a faithful representation, all the irreducible representations of the symmetry G are included in the above tensor product for a sufficiently large N .

Let us also label as $g_i \in \mathcal{V}$ the representation of the symmetry generator $g \in G$ on the site i . A symmetry G preserves the MBL phase if the local conserved quantities labeling, Eq.1.14, is consistent with the symmetry G then:

$$[\Pi_\alpha^{n_\alpha}, \prod_i g_i] = 0 \quad (2.1)$$

In that case the symmetry action factorizes on the local 1-bits, as:

$$\mathcal{V}_{n_{\alpha_1} \dots n_{\alpha_N}} = \mathcal{V}_{n_{\alpha_1}} \otimes \dots \otimes \mathcal{V}_{n_{\alpha_N}} \quad (2.2)$$

considering that the operators are strictly local.

2.2 Example of MBL phase preservation

An example[41] of local factorization of symmetry on the 1-bits is the MBL Ising paramagnet:

$$H = - \sum_{i=1}^L h_i \sigma_i^x + \dots \quad (2.3)$$

where the symmetry of the system is $G = \mathbb{Z}_2$ and the dots represent possible symmetry-preserving perturbations. The integrals of motion of the system are the σ_i^x and its eigenstates are a product state of definite $\sigma_i^x = \pm 1$. We can derive the local conserved projectors by a quasi-local unitary transformation U on σ_i^x , such as $\Pi_{\alpha_i}^{n=0,1} = U^\dagger \frac{1 \pm \sigma_i^x}{2} U$. The local action of the symmetry is given by:

$$\hat{g}_{\alpha_i} = U^\dagger \sigma_i^x U \quad (2.4)$$

Here \hat{g}_{α_i} commutes with the Hamiltonian H , $[\hat{g}_{\alpha_i}, H] = 0$, as they commute with all the conserved quantities $\Pi_{\alpha_i}^{n=0,1}$. Therefore, starting with a global symmetry $[\prod_i g_i, H] = 0$, the system factorizes into local symmetry for the MBL system

2.3 Non-abelian symmetries

Now let us assume that a system has a non-abelian symmetry G . In this case there are some irreducible representations of G that are necessarily multidimensional. This means that for an MBL state, there will be a multiplet structure, where local degrees of freedom cost no energy to excite, leading to the localization breaking[41].

In order to make the above argument clearer, we will assume that there is an MBL system with non-abelian symmetry G . We will conclude that such a case is not stable. In the 1-bit space, the Hilbert space has the form $\mathcal{H} = \otimes_\alpha \mathcal{V}_\alpha$, where the reducible representation \mathcal{V}_α can be decomposed as $\mathcal{V}_\alpha = \otimes_{n_\alpha=1}^{d_\alpha} \mathcal{V}_{n_\alpha}$. If the symmetry is non-abelian, some of the irreducible representations \mathcal{V}_{n_α} have dimension larger than 1. That means that we have to introduce an additional number $p_\alpha = 1, \dots, (\dim \mathcal{V}_{n_\alpha})$ to the quantum number n_α , in order to label an eigenstate. This leads to an exponential degeneracy of the eigenstates of the Hamiltonian.

As we saw above, the global symmetry is promoted to a local symmetry, as we assume that the system is in an MBL phase. Therefore, the local symmetry leads to local degeneracies, which results to an exponential-in-system-size degeneracy of all eigenstates. Such degenerate eigenstates are inherently unstable, even to infinitesimally small perturbations. This degeneracy can not be resolved, thus **either the symmetry or the localization must break down**. Whether the symmetry or the localization will break down considering a specific system depends on some simple principles.

2.4 General symmetry principles

The following symmetry constraints are based on this study [41]. First of all, in the case of *weak* disorder, we expect that the local excitations will overlap, leading the system always to thermalization.

The cases for a system with strong disorder are the following:

1. If the non-abelian symmetry group G has irreducible representations of bounded dimension, then there are two possible outcomes:
 - the system forms an MBL state in which symmetry is spontaneously broken down to an abelian subgroup [42].
 - the system forms a symmetry preserving quantum critical glass (QCG), an intermediate phase between thermalization and localization. Such a system cannot be described by a set of independent conserved quantities[43].
2. If the non-abelian symmetry group G is continuous, the irreducible representations are allowed to have an arbitrarily large dimension ($2S + 1$ for $SU(2)$). In this case the result is thermalization even for strong disorder[41].
3. If the symmetry group is abelian, then a stable MBL phase is allowed, as we saw in the \mathbb{Z}_2 example above.

We gather all the possible symmetry cases and their thermal/MBL expectations, in the table below:

group G	finite #irreps	#irreps $\rightarrow \infty$
$ \mathcal{V} = 1$	MBL allowed (\mathbb{Z}_n)	MBL allowed ($U(1)$)
$1 < \mathcal{V} < \infty$	MBL + Sym. Spont. Broken (or Quantum Critical Gases)	MBL + Sym. Spont. Broken
$ \mathcal{V} \rightarrow \infty$	-	only thermalization allowed

2.5 Systems with $SU(n)$ symmetry - what we know

Based on the discussion above, $SU(n)$ symmetries, being continuous and non-Abelian, are inconsistent with the MBL phase. However, it not obvious that thermalization is the only path that disordered $SU(n)$ symmetric systems follow, whatever the disorder strength. In fact, there are two previous studies on the $SU(2)$ disordered Heisenberg model [1, 44] that show evidence that this is not the case. The $SU(2)$ disordered Heisenberg model is defined in Chapter 3.

In a bit more detail, the authors claim that for sufficiently strong disorder $SU(2)$ symmetry allows an non-ergodic phase, although generally unstable, which lies between the thermal and MBL phase. ED results of the half-chain entanglement entropy till $L = 20$, Fig.2.1, show an non-ergodic behavior of systems under strong disorder. This ergodicity breaking behavior phenomenon disappears as we move to weaker disordered realizations, shown by the linear fit with the thermal expectation of the entanglement scaling with length.

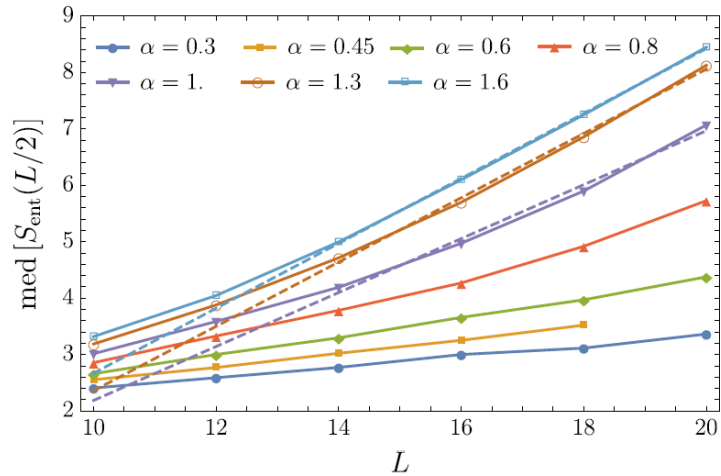


Figure 2.1: **plot taken from [1]**: Median value of the half-chain entanglement entropy for disorder strength $\alpha = \{0.3, 0.45, 0.6, 0.8, 1.0, 1.3, 1.6\}$ with respect to chain length. Linear fit shows the ergodic tendency of the weaker disorder realizations

Further analysis, using the SDRG method, offered an approximation concerning the chain length that is needed, so that we could see evidence of thermalization even with strong disorder. The authors claim, that for strong disorder, there is an *ergodization length scale*, L_{erg} , determined by the dashed line in Fig.2.2, after which spin resonances start to increase rapidly, leading the system, very slowly, towards thermalization.

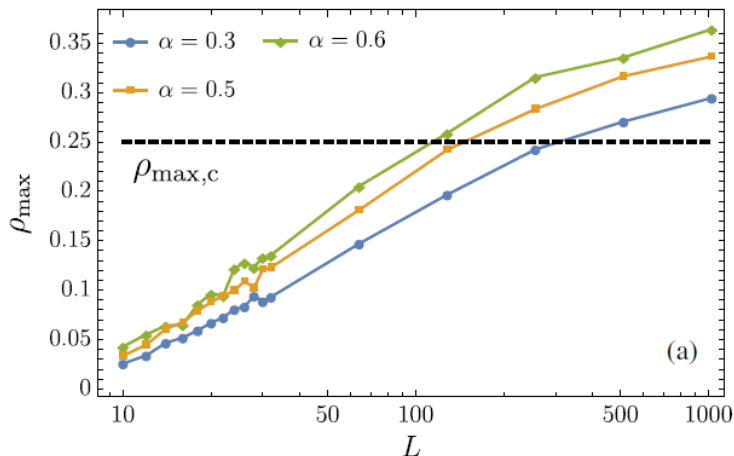


Figure 2.2: **plot taken from [1]**: Maximum density of the resonant spins developed in the course of SDRG as a function of system size

Based on the above claims, the non-ergodic phase is characterized as unstable, although the time scales are large enough for an experiment to observe ergodicity. In

our analysis we are able to achieve simulations for sizes close to the $L_{erg} \sim 100$ for disorder strength $\alpha = 0.5$, thus we will try to check if the above approximation seems reasonable.

Chapter 3

Time evolution of $SU(n)$ disordered Heisenberg chains

3.1 $SU(2)$ symmetric model

The model, we will study in this chapter, is the so called disordered Heisenberg chain with spin-1/2 sites, where $SU(2)$ symmetry holds. The Hamiltonian that describes the model, is the following:

$$H = \sum_i J_i \cdot \mathbf{S}_i \mathbf{S}_{i+1} \quad (3.1)$$

where \mathbf{S}_i are the spin operators ($\mathbf{S}_x, \mathbf{S}_y, \mathbf{S}_z$) and $J_i > 0$ the coupling constants between the sites in the antiferromagnetic case. We add the disorder in our model by letting the coupling constants J_i be drawn from the power-law distribution[45] (beta distribution for $b = 1$):

$$P(J_i) = \frac{\alpha}{J_i^{1-\alpha}}, \quad \text{with } 0 < J < 1 \quad (3.2)$$

The coupling distribution above appears naturally in low temperature studies and is consistent with earlier experimental results[46, 47].

Parameter α controls the disorder. In particular:

- small α (< 1) \rightarrow strong disorder
- large α ($\gtrsim 1$) \rightarrow weak disorder

Indeed, the disorder can be quantified by the ratio of two neighboring sites' couplings, as follows:

$$\frac{\max(|J_k|, |J_{k+1}|)}{\min(|J_k|, |J_{k+1}|)} = e^{1/\alpha} \quad (3.3)$$

It is clear from the equation above, that for small α the ratio becomes exponentially large. In the examples below, we will consider the $\alpha = 0.5$ case as *very strong* disorder and $\alpha = 1$ as *weaker* disorder. This distinction is also supported by a previous study of disordered Heisenberg chains with $SU(2)$ symmetry [1].

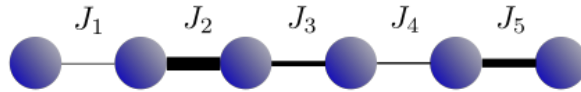


Figure 3.1: Cartoon of the coupling disorder

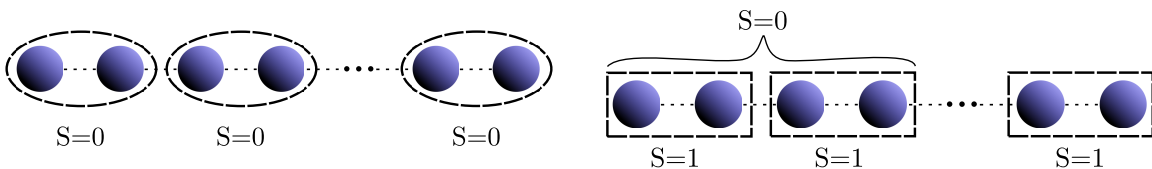
Setting

1. For a chain of L sites, we produce $L-1$ coupling constants J_i , drawn from the power law distribution above
2. We prepare an initial state $|\psi_{t=0}\rangle$ in the form of an MPS. We have considered two different initializations, one consisted of nearest neighbour singlet bonds, which belongs to the lower energy regime and one of nearest neighbour triplet bonds, which belongs to the high energy regime, roughly corresponding to an infinite temperature state.
3. We let the MPS evolve in time, using the tdDMRG method with Trotter time step $\delta\tau = 0.1$ and bond dimension $D = 1024$ or $D = 2048$, as we will describe later.

3.2 $SU(2)$ - Initialization

As mentioned above, we have chosen two different initial states, $|\psi(0)\rangle$, for the time evolution process:

- The first one is an MPS, which consists of a series of nearest neighbour singlets ($S_{tot} = 0$), keeping the total spin of the chain at 0.
- The second one is an MPS, where the nearest neighbour spins form a triplet state, in such a way that the total spin of 4 sites is 0. That way, the total spin of a chain with length multiple of 4 remains also 0.

Figure 3.2: The two $SU(2)$ initializations

When studying the MBL or thermal phase of a system, it is important to choose an energy range for the initial state close to the middle of the spectrum, where the density of states is sufficiently large. The time evolution process preserves the total energy of the system, therefore the time evolved states after any time t should have the same energy as the initial state. Away from the middle of the spectrum, convergence

to thermal phase becomes extremely slow. This can be also realized by the ETH ansatz:

$$\langle \alpha | \hat{O} | \beta \rangle = \mathcal{O}_{mc}(\bar{E}) \delta_{\alpha\beta} + e^{-S_{th}^{\bar{E}}/2} R_{\alpha\beta} f(\omega, \bar{E}) \quad (3.4)$$

The off-diagonal term of the ETH ansatz contains the factor $e^{-S_{th}^{\bar{E}}/2}$, where $S_{th}^{\bar{E}}$ is the thermodynamic entropy for energy E . This is analogous to the density of states. Therefore, the middle of the spectrum is usually chosen for ETH studies.

At this point, it is crucial to check in which energy range the two initial states, proposed above, live. For that, we produce 25 J-configurations for two different disorder strengths $\alpha = 1$ and $\alpha = 0.5$. For each one of them, we calculate the energy of the ground state of the particular Hamiltonian using the Density Matrix Renormalization Group (DMRG), described in section A.5. The highest energy of the spectrum is given by $E_{highest}(J) = -E_{gs}(-J)$, where $E_{gs}(-J)$ is the ground state of the Hamiltonian after taking $J \rightarrow -J$, computed again using the DMRG method. Then, we calculate the energy $\langle \psi_{init} | \hat{H} | \psi_{init} \rangle$ for both initializations and all J-configurations. The energy analysis results for the two disorder strengths are shown below:

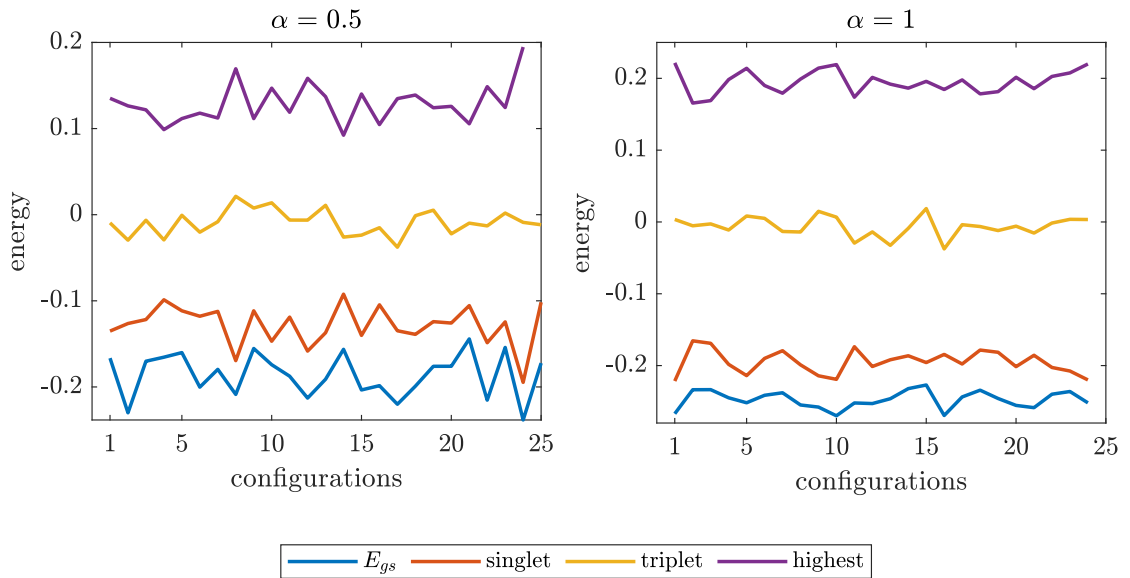


Figure 3.3: Energy of the ground state, the singlet initial state and the triplet initial state for 25 random J-configurations (25 random Hamiltonians) and $\alpha = \{0.5, 1\}$

From the energy analysis above, it is obvious that the nearest neighbour singlet initialization could be considered as a low-energy state, while the nearest neighbor triplet initialization as a high-energy state. As mentioned above, the high-energy regime is mostly preferable for ETH/MBL studies, thus the second initialization seems to be a better candidate.

3.3 $SU(3)$ symmetric model

The next goal of this project is to study the $SU(3)$ symmetric disordered Heisenberg model. The Hamiltonian describing the model has the same form as in the $SU(2)$ case:

$$H = \sum_{i,\alpha} J_i S_i^\alpha S_{i+1}^\alpha \quad (3.5)$$

with the difference that here the S_i^α are the $SU(3)$ spin operators referring to the λ_α generators of $SU(3)$ symmetry and the sum over α extends over these $N^2 - 1 = 8$ generators.

The 8 generators of $SU(3)$ can be written in a matrix form (Gell-Mann matrices) as:

$$\begin{aligned} \lambda_1 &= \begin{pmatrix} 0 & 1 & 0 \\ 1 & 0 & 0 \\ 0 & 0 & 0 \end{pmatrix} & \lambda_2 &= \begin{pmatrix} 0 & -i & 0 \\ i & 0 & 0 \\ 0 & 0 & 0 \end{pmatrix} & \lambda_3 &= \begin{pmatrix} 1 & 0 & 0 \\ 0 & -1 & 0 \\ 0 & 0 & 0 \end{pmatrix} \\ \lambda_4 &= \begin{pmatrix} 0 & 0 & 1 \\ 0 & 0 & 0 \\ 1 & 0 & 0 \end{pmatrix} & \lambda_5 &= \begin{pmatrix} 0 & 0 & -i \\ 0 & 0 & 0 \\ i & 0 & 0 \end{pmatrix} & \lambda_6 &= \begin{pmatrix} 0 & 0 & 0 \\ 0 & 0 & 1 \\ 0 & 1 & 0 \end{pmatrix} \\ \lambda_7 &= \begin{pmatrix} 0 & 0 & 0 \\ 0 & 0 & -i \\ 0 & i & 0 \end{pmatrix} & \lambda_8 &= \frac{1}{\sqrt{3}} \begin{pmatrix} 1 & 0 & 0 \\ 0 & 1 & 0 \\ 0 & 0 & -2 \end{pmatrix} \end{aligned} \quad (3.6)$$

For $SU(3)$ symmetry, we use locally the defining representation $(10) = \square$, where $q = (q_1 q_2)$ specifies the Young tableau as follows: q_1 is the offset of number of boxes from 1st to 2nd row and q_2 from 2nd to 3rd row.

Therefore, $\square = (10)$ and its dual $\square \square = (01)$.

For the $SU(3)$ model, we will discuss only the strong disorder regime with disorder parameter $\alpha = 0.5$. For that purpose, instead of generating new random coupling J-configurations, we will use the ones already generated for the $SU(2)$ model, as described in section 3.1, so that we can additionally compare the two models for each configuration separately for $L = 24, L = 48$ and $L = 96$.

3.4 $SU(3)$ - Initialization

Again, we will follow the same reasoning as in the $SU(2)$ case, described in section 3.2, in choosing a suitable initial state for our purpose. The main goal is to find an initial state with energy lying close to the middle of the spectrum ($E \sim 0$). The choice

of the subspaces for each site is also restricted by the fact that the total MPS has to be in the fully antisymmetric subspace, or $\begin{array}{|c|} \hline \square \\ \hline \square \\ \hline \square \\ \hline \end{array} = (\text{no box}) = (00)$ in the Young tableau notation.

By calculating the energy of different initial state realizations, we conclude that a suitable initial state can be constructed by choosing the subspaces shown below, for each 3 sites:

- 3-site multiplet: $q = (30)$, $\begin{array}{|c|c|c|} \hline \square & \square & \square \\ \hline \end{array}$ (fully symmetric subspace)
- 6-site multiplet: $q = (11)$, $[d = 8]$,
- 9-site multiplet: $q = (00)$, (no box)

The energy of the initial state above is around $E \sim -0.1$, tested for different random J-configurations.

3.5 Time-dependent Density Matrix Renormalization Group (tDMRG)

There is a variety of time-evolution methods based on tensor networks' techniques for initial matrix product states, like the Time-Dependent Block Decimation (TEBD), TEBD2, TEBD4 and Density Matrix Renormalization Group (DMRG) [48, 49]. For our time-evolution calculations we will use a powerful time-dependent DMRG (tDMRG)[50–52] code written by Andreas Weichselbaum using the QSpace tensor network library.

Algorithm

The tDMRG algorithm is based on the idea of combining the Trotter decomposition method and the DMRG algorithm (AppendixA). Assuming that the Hamiltonian describing the system is \hat{H} , we want to compute the time evolution of a state $|\psi\rangle$ by applying the time-evolution operator:

$$\hat{U} = e^{-i\hat{H}t} \quad (3.7)$$

to the initial state.

- As in the Trotter decomposition method, the first step is to separate the Hamiltonian into an odd and an even term, where the odd term refers to the odd bonds (1 – 2, 3 – 4, ...) and the even term to the even bonds (2 – 3, 4 – 5, ...) of the one dimensional chain. By introducing an infinitesimal time interval τ , the time-evolution operator Eq.3.7 takes the form:

$$\hat{U}(t) = (e^{-i(\hat{H}_{\text{even}} + \hat{H}_{\text{odd}})\tau})^N \approx (e^{-i\hat{H}_{\text{even}}\tau} e^{-i\hat{H}_{\text{odd}}\tau} + \mathcal{O}(\tau^3)) \quad (3.8)$$

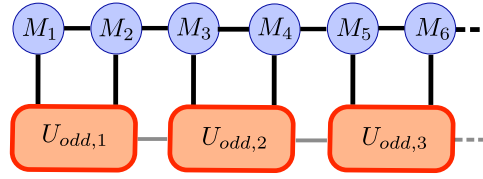


Figure 3.4: Odd-bond time evolution operators applied on the MPS

- By separating the Hamiltonian in odd and even terms, we have ensured that all the operators applied on odd (or even) bonds commute with each other. That is not the case for operators sharing the same site (H_{12} and H_{23} for example). Thus, we can construct an MPO for all the odd- (even-) bond operators and apply them at the same time Fig.3.4.
- We can start with applying the MPO referring to the $e^{-i\hat{H}_{odd}\tau}$ operators on all the odd bonds. After reshaping and applying SVD we end up to the updated tensors of each odd bond, Fig.3.5

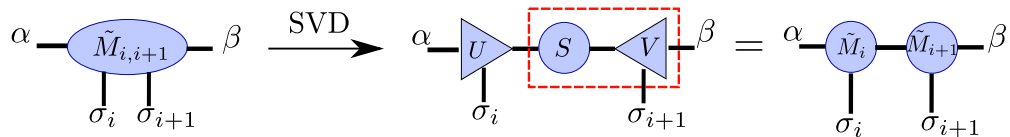


Figure 3.5: SVD step leading to the updated tensors

- The next step is where the DMRG ideas are applied. We need to variationally minimize the quantity:

$$||\psi(t + \tau)\rangle + |\psi_{compressed}\rangle|^2 \quad (3.9)$$

where $|\psi(t + \tau)\rangle$ is the MPS after the application of the odd-MPO, with bond dimension Dd and $|\psi_{compressed}\rangle$ is the compressed MPS with bond dimension D . This is done with one-site DMRG tensor updates and sweeps till the minimization is achieved.

- Finally, we apply the even-MPO to the compressed MPS and repeat the steps above.

Errors

While using the tDMRG algorithm it is crucial to monitor the error that affects the time-evolution of the MPS for each time t . In our case, we considered the calculation inaccurate at the point when the normalization of the state had fluctuations of the order of 10^{-6} . At that point, fluctuations to the total energy were becoming significant.

The tDMRG error is the result of two contributions:

1. Trotter error

The Trotter error is the result of the discretization of time into smaller time intervals. Thus, it grows with each step τ and linearly with time. We can reduce it by choosing smaller time intervals τ .

2. Truncation error:

The truncation error is the result of SVD truncation and grows exponentially with time, for the case that the entanglement entropy increases linearly with time. For strongly localized states we can, therefore, reach longer time scales.

For our time-evolution measurements, we monitor the impact of the above errors to the results by checking the normalization of the state for any time t and the total energy. As we will see later in the analysis of the results, the calculations are stopped at earlier times to secure accuracy of the results.

Chapter 4

Results and analysis

We apply the tDMRG method described above on the two initializations of the $SU(2)$ and $SU(3)$ symmetric disordered Heisenberg model to produce time-evolved states for different chain lengths and disorder strengths, which will be specified below. We can now make measurements of quantities of interest and study their dynamics over time.

4.1 Spin-spin correlations

The first promising candidate of such a measurement is the spin-spin correlations

$$\langle \psi(t) | \mathbf{S}_i \mathbf{S}_j | \psi(t) \rangle \quad (4.1)$$

where $|\psi(t)\rangle$ is the state of the system at time t , in our case the time-evolved MPS after time t , and \mathbf{S}_i the spin operator acting on site i . In our case the states $\psi(t)$ are not the eigenstates of the system, so we can not check the validity of the ETH (Eq.1.3). Instead, we will study how the spin-spin correlations relax over time, when disorder is presence.

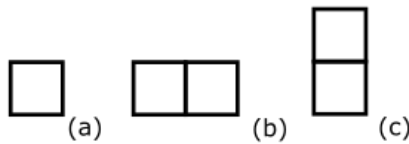


Figure 4.1: $SU(N)$ Young tableaux for (a) the defining irreducible representation that describes the spin of a site, (b) the symmetric and (c) the antisymmetric subspace of two such spins

Before analyzing the results, we should discuss about what values we expect from this calculation for $SU(N)$ quantum spin systems with local spins in the N -dimensional fundamental irreducible representation of $SU(N)$ (Fig.4.1). For an $SU(N)$ invariant state, the two site density matrix of dimension N^2 has a symmetric subspace of dimension $N(N + 1)/2$ and an antisymmetric subspace of dimension $N(N - 1)/2$.

Then the spin-spin correlations are given by:

$$\langle \mathbf{S}_i \mathbf{S}_j \rangle = \frac{1}{2} \left(p_S - p_A - \frac{1}{N} \right), \quad (4.2)$$

where p_S is the total weight of the state on the symmetric subspace and p_A on the antisymmetric subspace respectively.

Calculation of $\langle \mathbf{S}_i \mathbf{S}_j \rangle$ with tensor networks

The calculation of spin-spin correlations in the tensor network language is a trivial one. We first construct the MPO of the $\mathbf{S}_i \mathbf{S}_j$ by contracting the two 3-leg spin tensors that correspond to sites i and j respectively and contract it with the corresponding physical legs of the MPS. Then, we calculate the average of the operator by contracting the remaining open physical legs.

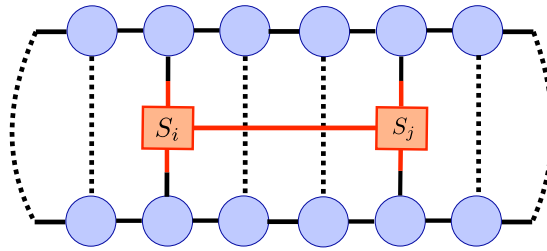


Figure 4.2: Spin-spin correlations calculation in tensor networks representation

$SU(2)$ symmetry

For $N = 2$ ($SU(2)$ symmetry), the value of the spin-spin correlations for a singlet bond (anti-symmetric subspace $p_A = 1$) is $-\frac{3}{4}$, while for a bond forming a triplet ($p_S = 1$) is $+\frac{1}{4}$. At infinite temperature $\langle \mathbf{S}_i \mathbf{S}_j \rangle \rightarrow 0$. A way to think about the infinite temperature limit, is to imagine that at $T \rightarrow \infty$ each spin-bond state will be a mixture of the singlet state and the three triplet states with equal probability, resulting to $\langle \mathbf{S}_i \mathbf{S}_j \rangle = \frac{1}{4} \cdot \left(-\frac{3}{4} \right) + 3 \cdot \frac{1}{4} \cdot \left(+\frac{1}{4} \right) = 0$.

The static spin-spin correlations for the second initialization chosen for $SU(2)$, as in Fig.3.2, and an $L = 24$ chain is shown in Fig.4.3

The 4-spin triplet structures described in Fig.3.2 are represented in the color-plot below as colored “islands”. Indeed, the red squares represent the triplet bonds with $\langle S_i S_{i+1} \rangle = +1/4$, while the blue squares with $\langle S_i S_{i+1} \rangle = -0.5$ are the additional spin-spin correlation needed, so that the 4-spin block has total spin equals 0.

$SU(3)$ symmetry

For $N = 3$, Eq.4.2 gives the expected $\langle S_i S_j \rangle$ values for the fully symmetric and anti-symmetric subspaces. In particular, $\langle S_i S_j \rangle = -\frac{2}{3}$ for the anti-symmetric subspace

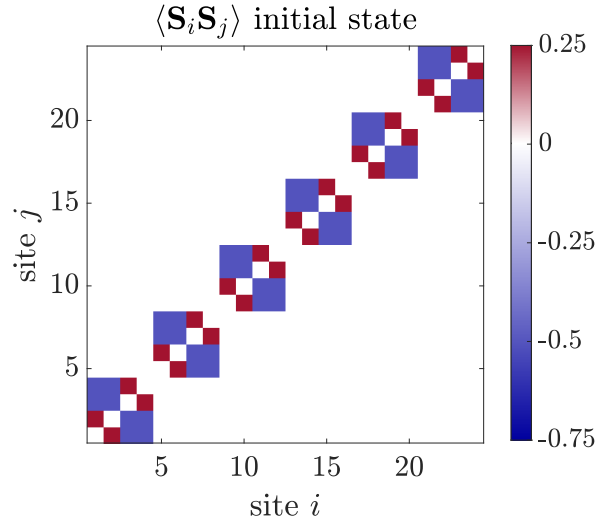


Figure 4.3: $\langle S_i S_j \rangle - 3/4\delta_{ij}$ colorplot for the $SU(2)$ initial state

and $\langle S_i S_j \rangle = \frac{1}{3}$ for the anti-symmetric subspace.

The spin-spin correlations colorplot for the initial state, as described in section 3.4, can be seen in Fig.4.4.

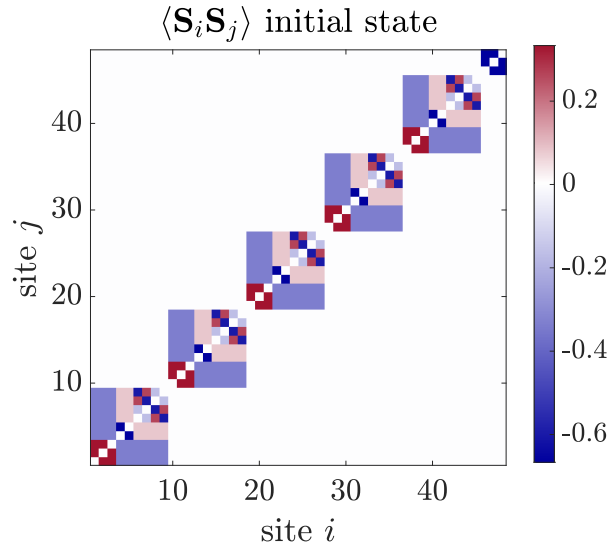


Figure 4.4: $\langle S_i S_j \rangle - 3/4\delta_{ij}$ colorplot for the $SU(3)$ initial state

Here, the 9-spin structures are more complicated as many subspaces are involved. Nevertheless, the fully (anti-)symmetric two-site bonds can be seen, like the fully symmetric $(2, 3)$ -bond for each 9-site structure for example.

Dynamics

The behavior and dynamics of a random Heisenberg chain as it evolves through time can be qualitatively revealed by tracking the equal-time spin-spin correlations as time evolves. The examples we mention below refer to $SU(2)$ symmetric systems, but the same ideas apply for $SU(3)$ symmetric ones, taking into account that the spin-spin correlations values describing each subspace are different. Nevertheless, the information we obtain remains the same.

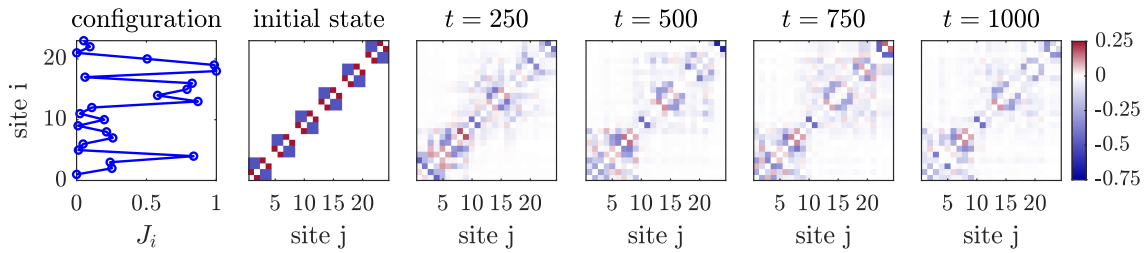


Figure 4.5: Left plot: Coupling constant J_i 's random configuration. Plots 2-6: Color-plots of the $\langle S_i S_j \rangle - 3/4\delta_{ij}$ correlations for the time evolution of a $L=24$ spins system ($\alpha = 0.5$)

In Fig.4.5 we can see how the spin-spin correlations evolve in time for an $L = 24$ size random Heisenberg spin chain. As mentioned above, the initial localized state is characterized by non-zero nearest- and next nearest- neighbour correlations. In this example, as the system evolves, we observe the delocalization of the majority of the bonds, plus longer range correlations appear. In the final picture at $t = 1000$, there are no singlet or triplet localized bonds, rather most of the bonds have $\langle S_i S_{i+1} \rangle$ correlations around 0.

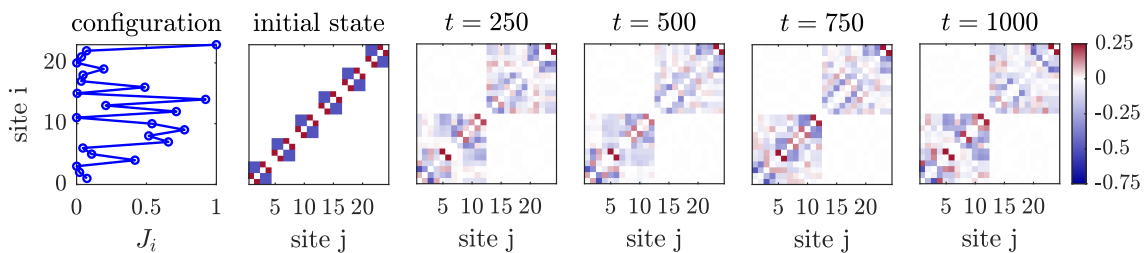


Figure 4.6: Left plot: Coupling constant J_i 's random configuration. Plots 2-6: Color-plots of the $\langle S_i S_j \rangle - 3/4\delta_{ij}$ correlations for the time evolution of a second $L=24$ spins system ($\alpha = 0.5$)

Analysis of the spin-spin correlation color-plots for different random J -configurations reveal a second path that disorder $SU(2)$ symmetric Heisenberg systems could follow.

Choosing a second $L = 24$ configuration and same disorder strength $a = 0.5$, shown in Fig.4.6, one can notice that the behaviour of the system is different from the previous example.

In this example, we notice that there are certain bonds (bond between spins 6 and 7 for example), that preserve their $\langle S_i S_{i+1} \rangle$ over time, meaning they remain localized in the same state (the triplet state in that bond case). In fact, we can also notice that this particular system is separated in two smaller subsystems that evolve independently, without “communicating” with each other. Thus, longer range correlations for spins between these two subsystems are 0 (white off-diagonal areas).

4.2 Eigenvalues of spin-spin correlations

Inspired by this study [53] of a fermionic system, it seems interesting to examine the behaviour of the eigenvalues of the spin-spin correlations matrix $\rho_{ij} = \langle S_i S_j \rangle$ we have already calculated above. In their work [53], the authors studied a system of spinless fermions with nearest neighbor hopping and repulsive interaction in a disordered lattice. In order to characterize their states $|\psi(t)\rangle$ they calculate the one particle density matrix, defined as:

$$\rho_{ij}(t) = \langle \psi(t) | c_i^\dagger c_j | \psi(t) \rangle \quad (4.3)$$

and then diagonalized it.

The eigenvalues calculated are the occupation numbers and the eigenfunctions are the natural orbitals of the fermionic system. Studying the time evolution of the eigenvalues of ρ_{ij} as seen in Fig.4.7, the authors distinguish between thermal and MBL phase by the nature of their relaxation dynamics. In particular, the eigenvalues relax slowly to values different than 0.5 for strong disorder systems at the MBL phase, while they approach the 0.5 value for weak disorder systems moving towards the thermal phase.

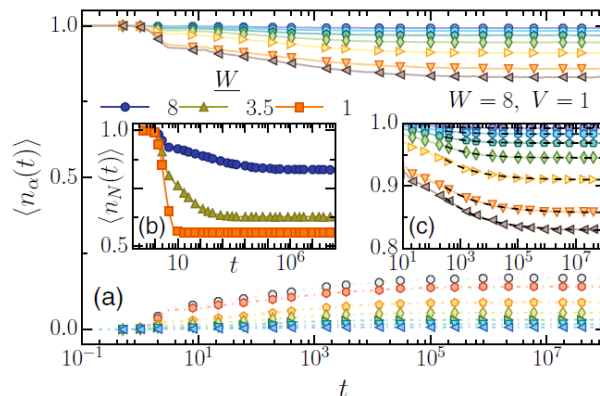


Figure 4.7: **plot taken from [53]**: Main panel (a): Time evolution of disorder-averaged occupation spectrum n_α deep in the MBL phase, (b) for both MBL and thermal phase, (c) Power-law relaxation for the upper half of the spectrum

For our problem, instead of calculating the one particle density matrix, we calculate the spin-spin correlation matrix, defined as:

$$\rho_{ij}(t) = \langle \psi(t) | \mathbf{S}_i \mathbf{S}_j | \psi(t) \rangle \quad (4.4)$$

and then we diagonalize it. The connection between 4.3 and 4.4 becomes more direct after a Jordan-Wigner transformation, in particular, if a Jordan-Wigner string is included in 4.4 in between sites i and j . Further analysis of this topic will be done outside this master project.

The relaxation dynamics of the eigenvalues of ρ_{ij} for the two cases studied in the previous section (Fig.4.5 and Fig.4.6) can be seen in Fig.4.8 and Fig.4.9.

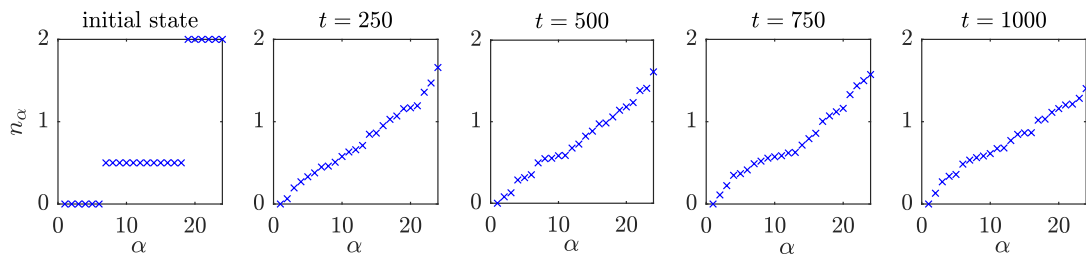


Figure 4.8: Time evolution of the eigenvalues n_α of ρ_{ij} for the Fig.4.5 configuration

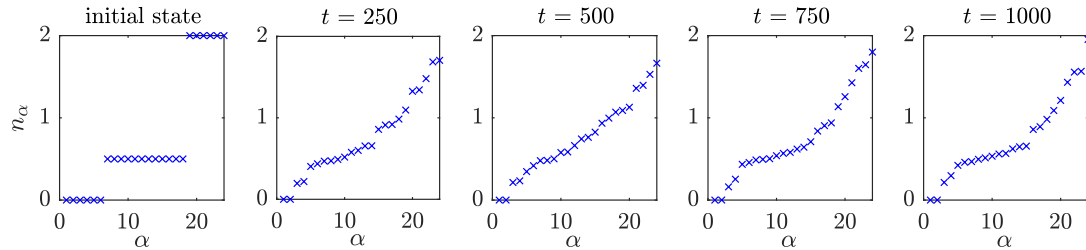


Figure 4.9: Time evolution of the eigenvalues n_α of ρ_{ij} for the Fig.4.6 configuration

The initial state is characterized by a gaped eigenvalue spectrum, where the eigenvalues take values $n_\alpha = 0$ coming from the uncorrelated bonds, $n_\alpha = 2$ from the triplet bonds and $n_\alpha = 0.5$ from the rest of the bonds. The relaxation dynamics of the eigenvalues show a different behaviour for a system that gets delocalized, Fig.4.8, and one that does not, Fig.4.9. First, we notice that in both cases the eigenvalues cover almost the whole spectrum. The difference is that for the delocalized case the spectrum becomes uniform and moves towards smaller values, while for the localized case, the eigenvalue spectrum shows gaps, as bonds and blocks of bonds remain localized to a particular state through time. Although there is a fast relaxation from the initial state ($t = 0$ to $t = 250$) the most of the eigenvalues, in the localized case, reach a saturated value in the end ($t = 750$ to $t = 1000$).

4.3 Averaging over disorder

4.3.1 Parameters

So far, we have taken a first look at the different paths disordered Heisenberg models can follow, by arbitrarily choosing two examples of realizations. At this point of the analysis, it is time to study how the behavior and dynamics of disordered Heisenberg systems depend on parameters of the problem. We will present an analysis of the time evolution of such systems over two parameters:

- system size L
- disorder strength α

As we deal with disorder, such an analysis demands averaging over different disorder realizations, meaning different random J-coupling configurations, for each parameter case. We choose 3 chain length cases $L = \{24, 48, 96\}$ and two disorder realizations $\alpha = \{0.5, 1\}$ to cover both the strong and weaker disorder regime.

4.3.2 Nearest-neighbor spin correlations $\langle \mathbf{S}_i \mathbf{S}_{i+1} \rangle$

As we saw in section 4.1 spin-spin correlations give a quantitative picture of the dynamics of a disordered Heisenberg chain as it evolves in time. Now, we have to find a way to use this measurement and averaging over disorder to analyze the behavior of such systems for different L and α realizations. For that we can focus only on the nearest-neighbor spin-spin correlations $\langle \mathbf{S}_i \mathbf{S}_{i+1} \rangle$, studying the behaviour of each 2-spin bond as a result of the nearest neighbor interactions of the spins.

In a similar work, [1], the authors use the SDRG method to study disordered Heisenberg chains. They calculate the averages of two local observables $\hat{O}_{max} = \mathbf{S}_i \mathbf{S}_{i+1}$ and $\hat{O}_{rand} = \mathbf{S}_j \mathbf{S}_{j+1}$ over eigenstates. \hat{O}_{max} refers to the bond which is most strongly coupled, while \hat{O}_{rand} to a random coupled pair, in the SDRG picture. That way they are testing the ETH validity or breakdown for different disorder strengths and $L = 22$ long chains. The results are presented in Fig.4.10.

In our case, we have no knowledge of the eigenstates of the system. Instead, the results of the tdDMRG procedure are time-evolved states $|\psi(t)\rangle$. The average of a local observable, like $\hat{O} = \mathbf{S}_i \mathbf{S}_{i+1}$, over the state $\psi(t)$ is connected to the ones over the eigenstates of the system at infinite temperature, in the following way:

$$\langle \psi | \mathbf{S}_i \mathbf{S}_{i+1} | \psi \rangle_\infty = \sum_{\alpha} p_{\alpha} \langle \alpha | \mathbf{S}_i \mathbf{S}_{i+1} | \alpha \rangle \quad (4.5)$$

We will check the ergodicity of a random Heisenberg chain of length L characterized by disorder strength α by calculating the observable $\langle \psi | \mathbf{S}_i \mathbf{S}_{i+1} | \psi \rangle$ for all the bonds of the chain, time-averaged in a time window $t = 850 - 1000$. Then, we repeat the same calculation for different configurations of same parameters L and α . We include the results for each (L, α) realization in normalized histograms, as in Fig. 4.11.

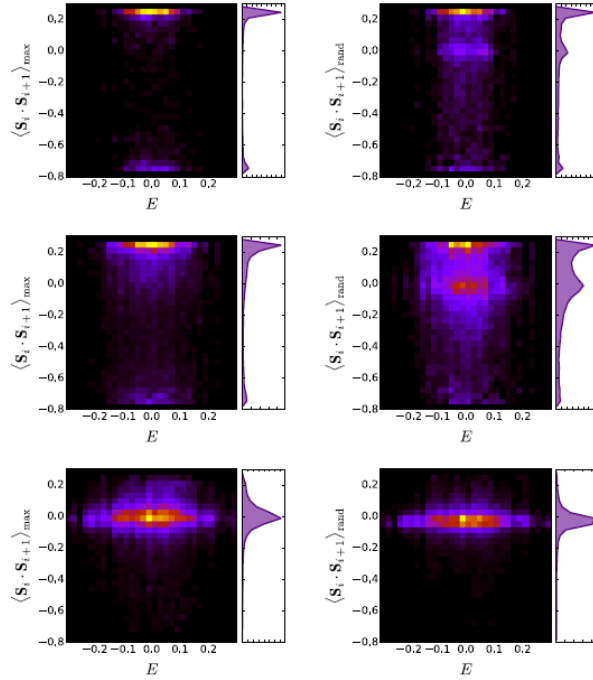


Figure 4.10: **plot taken from [1]**: Heat maps for the distributions of $\langle \alpha | \hat{O}_{max} | \alpha \rangle$ (left column), $\langle \alpha | \hat{O}_{rand} | \alpha \rangle$ (right column) for > 25000 eigenstates, $L = 22$ and $\alpha \in 0.3, 0.6, 1.3$ using the SDRG method

Expectations

The initial state consists of triplet bonds with $\langle \mathbf{S}_i \mathbf{S}_{i+1} \rangle = +0.25$, uncorrelated bonds between the 4-site triplet structures with $\langle \mathbf{S}_i \mathbf{S}_{i+1} \rangle = 0$ and bonds with $\langle \mathbf{S}_i \mathbf{S}_{i+1} \rangle = -0.5$ between two triplet bonds, which are needed to achieve total spin $S_{tot} = 0$ every 4 spins. For localized systems, that break the ergodicity, we expect triplet bonds to remain localized, meaning initially triplet bonds with $\langle \mathbf{S}_i \mathbf{S}_{i+1} \rangle$ conserved over time. If the system is ergodic, the spin-spin correlations of most of the bonds should have values around the thermal average of the observable, which for $\langle \mathbf{S}_i \mathbf{S}_{i+1} \rangle$ is 0 for $T \rightarrow \infty$.

Analysis

Starting with the strong disorder case ($\alpha = 0.5$), for $L = 24$ and $L = 48$ we can clearly distinguish two peaks: the one at $\langle \mathbf{S}_i \mathbf{S}_{i+1} \rangle = +0.25$ and a wider one around $\langle \mathbf{S}_i \mathbf{S}_{i+1} \rangle = 0$. This behaviour is evidence of ergodicity breakdown as a significant number of nearest neighbour spin bonds remain localized in their initial triplet case. On the contrary, the triplet bar becomes insignificant for the case of $L = 96$. In that case, there are signs of the system's tendency towards the thermal regime.

The picture is much more obvious for the weaker disorder case ($\alpha = 1$). For weaker disorder, the system show evidence of ergodic behavior for all lengths studied, as the histogram bar referring to localized bonds is quite insignificant.

The results for $L = 24$, for both disorder strengths, seem to agree with the spin-

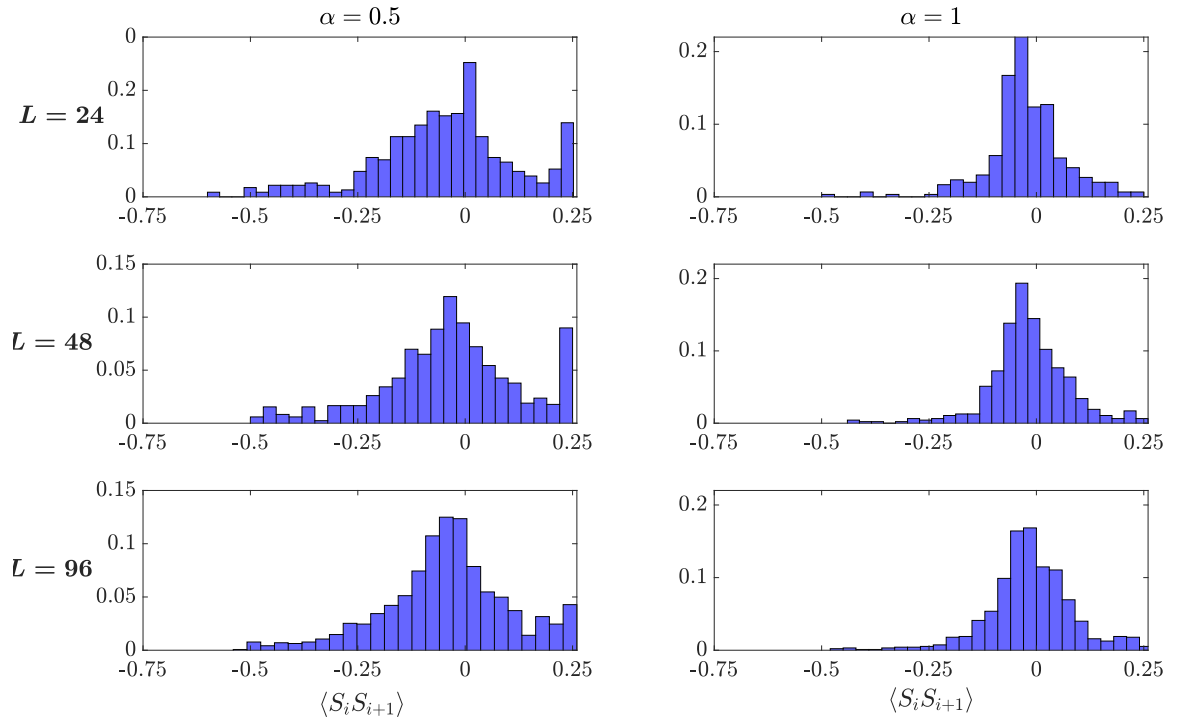


Figure 4.11: Normalized histograms of the nearest neighbor spin-spin correlations for 20 configurations and $\alpha = \{0.5, 1\}$, $L = \{24, 48, 96\}$.

spin correlation calculations done using the SDRG method (histograms in Fig.4.10 for $L = 22$). For small sized systems, strong disorder breaks ergodicity, preventing blocks of different sizes from getting delocalized, as we will see in the next chapters. The affect of strong disorder seems to fade out as the system sizes become larger and the finite size effects are diminished.

4.4 Entanglement entropy scaling

A second indicator of ergodic/nonergodic behaviour, commonly used, is the scaling of the entanglement entropy with system size. As mentioned in previous chapters, the entanglement entropy is expected to obey a volume law for thermalizing systems, while it follows an area law for systems into the MBL phase. The method, that is frequently used, is the calculation of the half-chain entanglement entropy. The states in the middle of the chain have to satisfy $S_{ent}(L/2) \sim L/2$ for systems in the thermal phase. Scaling with system length slower than the above, is an indication of non-ergodic behaviour. However, in our case, the fact that we study realizations of only 3 different lengths ($L = 24, 48, 96$) and the fact that our systems are adequately large, allows us to use a different approach to study the scaling of the entanglement entropy.

Cut Averaged Entanglement Entropy (CAEE)

In a work in 2016 [54], the authors introduced cut-averaged entanglement entropy as a way to quantify MBL phase at the level of a single eigenstate. This method has also been used in a study of disordered spin chains with finite non-Abelian symmetry [55].

Starting with a single state $\psi(t)$ at time t , as the result of the time evolution of the initial state and a random J-configuration, we calculate the block entanglement entropy of **all** the subsystems of size l . Then, we average over the subsystems of the same size. We repeat this procedure for as large subsystem lengths l as we can afford. The result of this method is a block entanglement entropy curve as a function of subsystem length, where each curve refers to a single random realization.

Calculation of CAEE with tensor networks

As described above, we would like to calculate the block entanglement entropy of all the l -site subsystems of our L -site system, for as a large l value as we can computationally afford. In order to reduce the finite-size effects in our calculation, we discard the first $L/6$ sites from the left border of the chain and the last $L/6$ sites from the right border of the chain.



Figure 4.12: Part of the chain we consider for the entanglement entropy calculation

The entanglement entropy of a subsystem A, with respect to the rest of the system, let us call it B, is given by:

$$S(\rho_A) = -\text{Tr}(\rho_A \log \rho_A) \quad (4.6)$$

where ρ_A is the reduced density matrix referring to subsystem A:

$$\rho_A = \text{Tr}(\rho_{AB}) \quad (4.7)$$

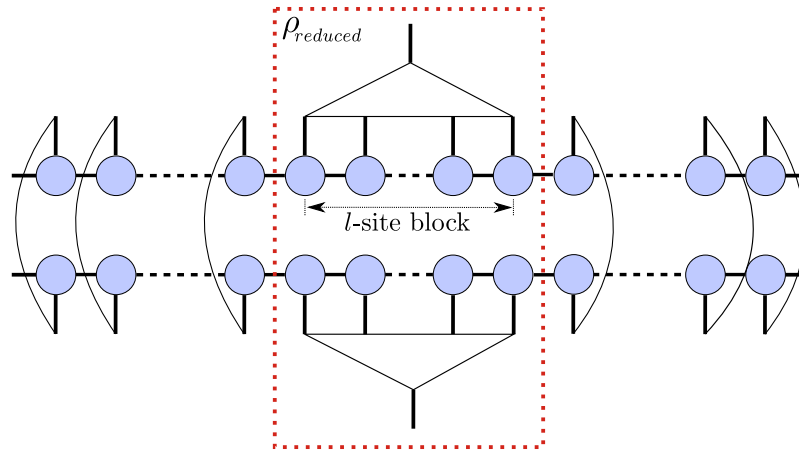


Figure 4.13: Calculation of the reduced density matrix of an l -site block (subsystem A), by tracing out the rest of the sites, in the tensor networks representation

Thus, the first step is to calculate the reduced density matrix of an l -site block living somewhere in the chain. For that, we need two copies of the MPS, Fig.4.13. The tracing out of subsystem B is achieved by *contracting* the physical legs of each M_i^\dagger and M_i pair of tensors. Then, we turn subsystem A (l -site block) into a matrix by *fusing* all the l physical legs of the tensors which are part of A. The processes above lead to a 2-leg tensor, which is the reduced density matrix referring to subsystem A, ρ_A . Next, we diagonalize the reduced density matrix, calculate the $\log \rho_A$ and calculate the trace of Eq.4.6 by contracting the ρ_A with the $\log \rho_A$ matrix.

Finally, we repeat the above calculation for the l -site blocks contained in the colored area defined in Fig.4.4.

The results of the block entropy measurement for $SU(2)$ symmetric systems and $\alpha = \{0.5, 1\}$, $L = \{24, 48, 96\}$ are shown below.

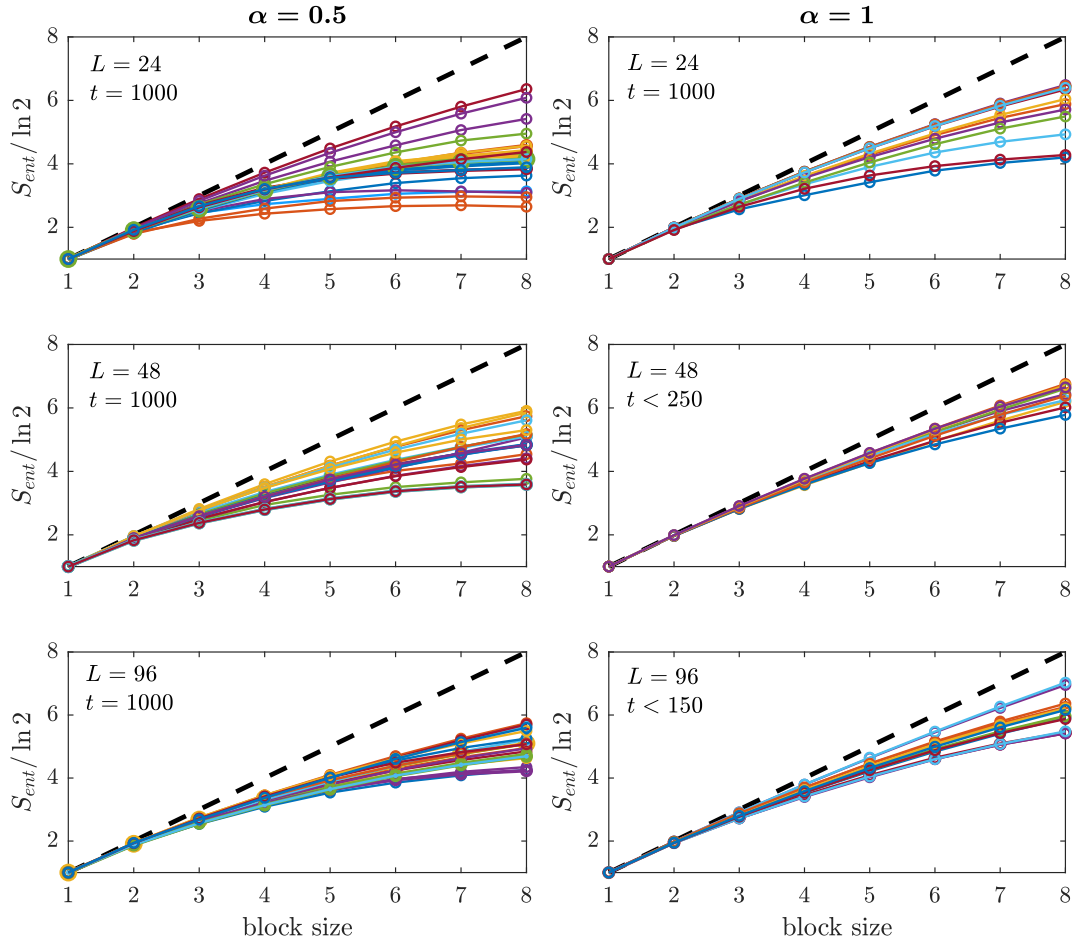


Figure 4.14: Entanglement entropy $S_{ent}/\ln 2$ scaling with subsystem size for ~ 20 configurations and $\alpha = \{0.5, 1\}$, $L = \{24, 48, 96\}$. Each colored line refers to a single chain with random J . The black dashed line is the entanglement entropy scaling with system length for the ergodic regime

Expectations

The slope of each of the block entanglement entropy curves, $\Delta S/\Delta l$, reveals the entropy scaling of the particular configuration with length. The expectation of the scaling for the ergodic regime is $S_{ent}(l) \sim l$, which corresponds to a slope equal to 1, while the MBL phase to a slope equal to 0. The dashed line drawn on the plots in Fig.4.14 is the thermal expectation of the entanglement scaling with length.

Analysis

Let us start with the 3 plots in Fig.4.14 referring to the strong disorder case ($\alpha = 0.5$). For $L = 24$ we notice that the curves referring to different strong disorder configurations show a significant variance from the mean value, or spreading, which seems to become less significant as we move to larger chains. There are reports [28] that connect the variance of the entanglement entropy to the thermal-MBL transition. In particular, the maximum value of the variance is at the transition point and it reduces as we move away from it and towards either the thermal or MBL phase. There is no thermal-MBL transition in this case, as continuous non-Abelian symmetries do not support MBL. Nevertheless, that spreading could be an indication of the system's tendency to move away from the ergodic regime for small chain lengths.

Keeping the point on the variance on hold, we will focus now on how the entanglement curves diverge (their slope) from the thermal expectation (slope = 1). It is important to note that all the simulations lasted till $t = 1000$. So a reasonable question is whether that time interval is enough for all the 3 different length realizations to relax to their final state. For that, we plot the time evolution of the entanglement entropy corresponding to the 8-site blocks for $L = 96$, Fig.4.15. The right plot of Fig.4.15 indicates that the majority of the configurations have not reached their final evolved state at $t = 1000$. This means that the points of the entropy lines for the $L = 96$ case are underestimated.

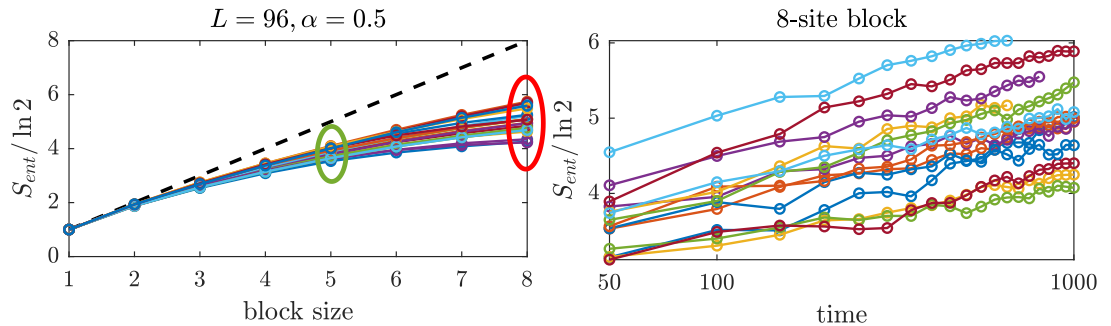


Figure 4.15: Time evolution of the entanglement entropy of the 8-spin blocks (red circle) for different random configurations ($L = 96$, $\alpha = 0.5$). The time evolution of the 5-spin blocks (green circle) is depicted in Fig.4.16.

Similarly, the time evolution of the entanglement entropy referring to 5-spin blocks is presented in Fig.4.16, for different chain lengths. For $L = 24$ and the majority of the realizations, the entanglement entropy shows signs of saturation over time. On the contrary, the $L = 96$ case shows a constant, but slow, increase for all the random configuration, which is in agreement with the behavior of the entanglement entropy concerning the 8-site blocks in Fig.4.15. Further analysis of the entropy scaling with time is a topic of future study outside this project.

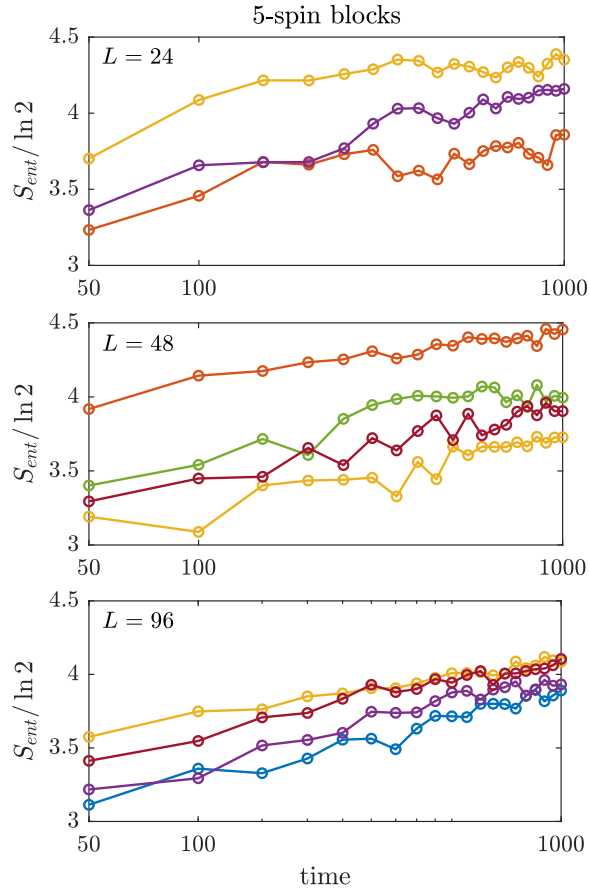


Figure 4.16: Time evolution of the entanglement entropy of the 5-spin blocks for different random $\alpha = 0.5$ configurations for $L = \{24, 48, 96\}$

Combining the two arguments above, about the variance and slope, we can make the following claims. For $L = 24$ the significant variance of the slopes of the entanglement lines indicate that the system is far from either the thermal or MBL state, which implies that there is **ergodicity breaking**. This claim is in agreement with the ED results presented here [1] for small chains and disorder strength $\alpha = 0.5$, as well as with the spin-spin correlation results we presented in Section 4.3.2. Moving towards larger chain sizes, indications that the systems lean towards an ergodic behavior appear.

The picture for the weaker disorder regime ($\alpha = 1$) seems more profound. Even for small systems, $L = 24$ with weaker disorder, the entanglement entropy slopes tend to cover larger values and smaller variances. This is a sign of the ergodicity breaking disappearance, which was present in the strong disorder regime. The above observations are in agreement with the ED calculation done here [1]. For larger chains and weaker disorder the evidence of thermalization is even stronger, as expected.

4.5 $SU(2)$ vs $SU(3)$ symmetry

The next question that arises is what is the role of symmetry on the ergodic or non-ergodic behavior of random Heisenberg chains. Starting from the $SU(3)$ initial state, described in Section 3.4, we produce time-evolved states, using the tdDMRG method, the same way we did for the $SU(2)$ symmetric model earlier. We will consider only the strong disorder regime for $\alpha = 0.5$. It is important to note that we use exactly the same random J-configurations, as the ones for the $SU(2)$ case, for each $L = \{24, 48, 96\}$ respectively. The quantities measured are also the same: nearest neighbor spin-spin correlations and block entanglement entropy.

4.5.1 Nearest-neighbor spin correlations $\langle \mathbf{S}_i \mathbf{S}_{i+1} \rangle$

The results of the spin-spin correlations' measurement for the strongly disordered $SU(3)$ symmetric model and chain lengths $L = 24, 48, 96$ are shown in Fig.4.17.

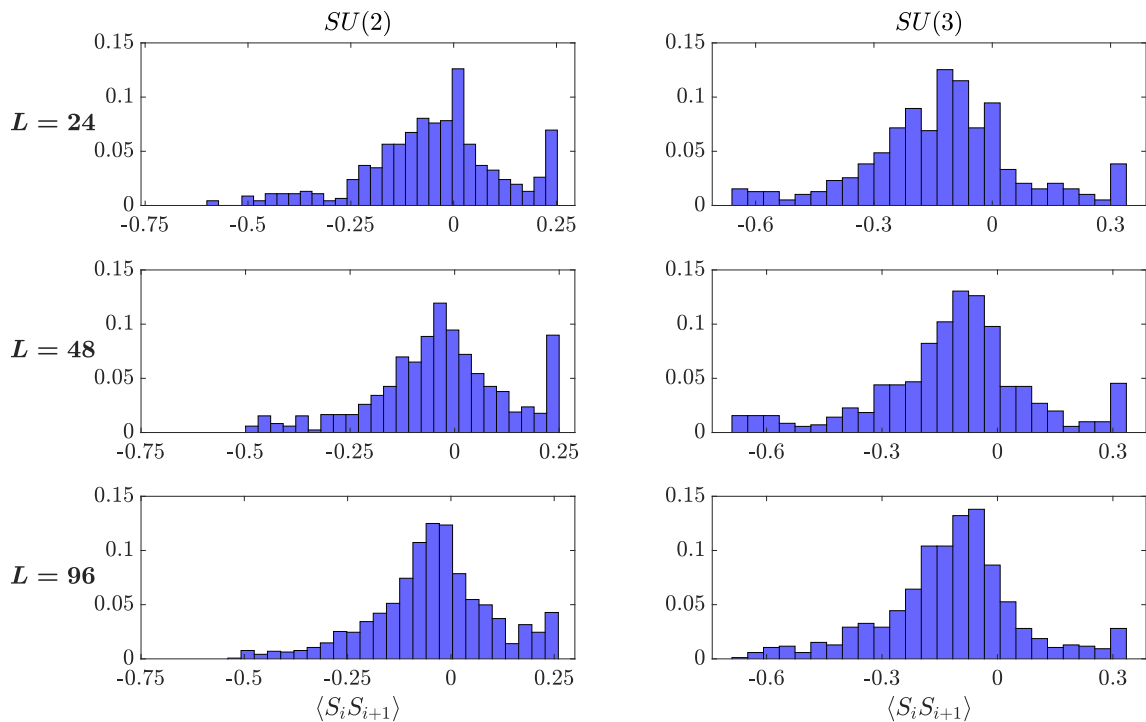


Figure 4.17: Normalized histograms of the nearest neighbor spin-spin correlations for ~ 20 configurations for the $SU(2)$ and $SU(3)$ symmetric model and $\alpha = 0.5$, $L = \{24, 48, 96\}$

Expectations

The initial state of the $SU(3)$ model, discussed in Section 3.4 and 4.1, consists of localized bonds both in the fully symmetric and fully anti-symmetric subspace. These bonds correspond to values $\langle \mathbf{S}_i \mathbf{S}_{i+1} \rangle = +1/3$ and $\langle \mathbf{S}_i \mathbf{S}_{i+1} \rangle = -2/3$ respectively. Thus,

in the case of ergodicity breaking, we expect the histogram bars referring to these values to remain significant.

Analysis

In Fig.4.17 we also present the $SU(2)$ results discussed in the previous sections. Even for the small chains of lengths $L = 24$ and $L = 48$, the $SU(3)$ histograms show that the ergodicity breaking phenomenon is reduced. In particular, the bars representing the localized bonds at $\langle \mathbf{S}_i \mathbf{S}_{i+1} \rangle = +1/3$ and $\langle \mathbf{S}_i \mathbf{S}_{i+1} \rangle = -2/3$ reveal that the percentage of the localized bonds is below 5% of the total bonds in each case. The same picture is present for the case of $L = 96$, but in this case $SU(2)$ was already showing evidence of ergodicity. The interesting result lies on the small chains, where symmetry affects the ergodicity breaking seen in the $SU(2)$ case.

4.5.2 Entanglement entropy scaling

In Fig.4.18, we present the entanglement entropy scaling results of the $SU(3)$ symmetric model accompanied with the results for $SU(2)$ symmetry already shown.

Again, the small size chains show a different behavior as we move to $SU(3)$ model. Firstly, the spreading of the $SU(3)$ lines becomes smaller than the corresponding $SU(2)$ lines for the same lengths L . Additionally, the same random realizations that were showing entanglement entropy scaling away from the thermal expectation (smaller slopes) have moved towards the thermal expectation (larger slopes). This is a sign of the ergodicity breaking becoming less significant, as we saw from the spin-spin correlation results. The $L = 96$ results show small difference between the two symmetries as expected.

$SU(3)$ symmetry has an impact on the relaxation time scaling of the disordered systems. Due to calculation error restrictions, caused by limited bond dimension, the time interval of the time evolution for each $SU(3)$ case (Fig.4.19) is significantly smaller than the one for the $SU(2)$ cases as the system size increases. For the $L = 96$ case, where the systems show similar, close to ergodic, behavior the relaxation times are not the same. In particular, it is significantly smaller for the $SU(3)$ symmetric model, as shown in Fig.4.18. The relaxation dynamics differences between the two symmetries would be an interesting topic for further studying.

Nevertheless, the results shown above provide evidence that $SU(3)$ symmetry is inconsistent with ergodicity breaking, at least in the parameter regimes studied, where $SU(2)$ supports it. In an experiment, where time scales are limited, these two different ergodicity behaviors would be very clear to distinguish. Still, a better analysis is necessary concerning the scaling of the entanglement entropy with time to make these claims stronger, as for the $SU(3)$ symmetric model the time interval of the simulation is limited by computational restrictions.

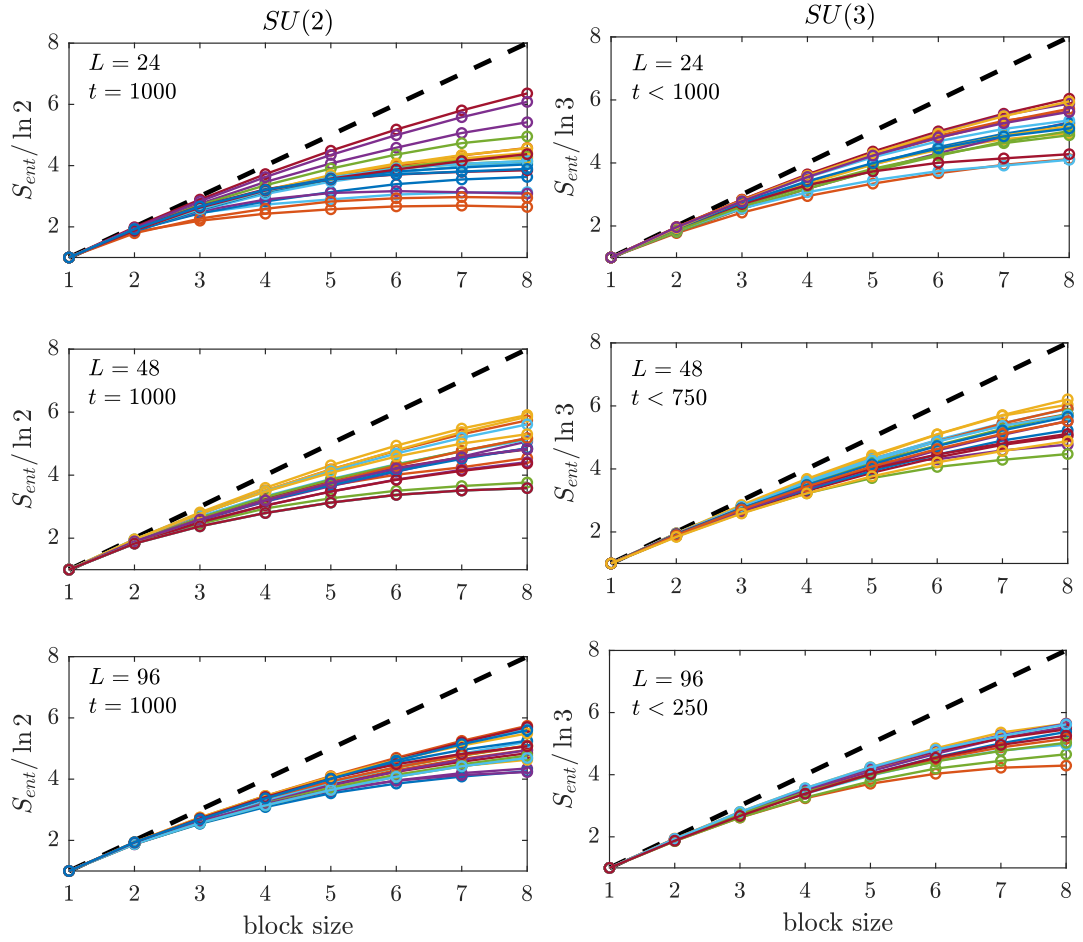


Figure 4.18: Entanglement entropy $S_{ent}/\ln 2$ scaling with subsystem size for the same ~ 20 configurations and $SU(2), SU(3)$ symmetry, $L = \{24, 48, 96\}$. Each colored line refers to a single chain with random J . The configurations used for the $SU(3)$ symmetric Hamiltonians are the same as for the $SU(2)$ ones. The black dashed line is the entanglement entropy scaling with system length for the ergodic regime

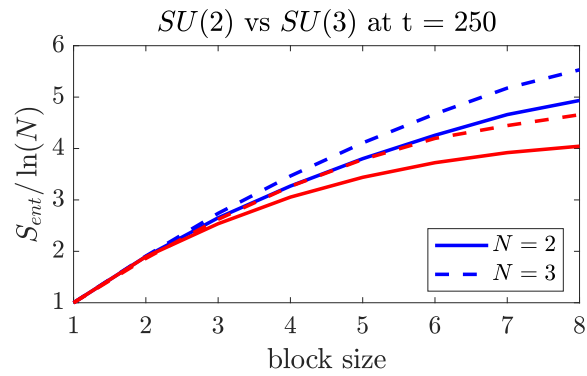


Figure 4.19: Entanglement entropy scaling with subsystem length. Same color lines refer to the same random J-configuration for $\alpha = 0.5$, solid lines to the $SU(2)$ symmetric model and dashed lines to the $SU(3)$ model

4.6 Dynamics of sub-thermal regime

The analysis of the spin-spin correlations and entanglement entropy scaling results shows evidence of ergodicity breaking, present for $SU(2)$ symmetric strongly disordered Heisenberg chains of small sizes, which disappear for the $SU(3)$ symmetric model. It would be interesting to understand the dynamics behind this behavior, as it lies between the already well-studied thermal and MBL phase. The MBL phase is described by quasi-local operators which commute with the Hamiltonian. There are assumptions that the sub-thermal regime is characterized by localized blocks of varying sizes, or in other words, integrals of motion of varying locality [1].

To check that, we will consider two examples of disordered realizations of size $L = 24$ and strong disorder, which is in the parameter regime we observe the breaking of ergodicity. By calculating the spin-spin correlation colorplot referring to the final state of the random realizations, Fig.4.20 and Fig.4.21, it is easy to spot bonds that have remained localized at $t = 1000$.

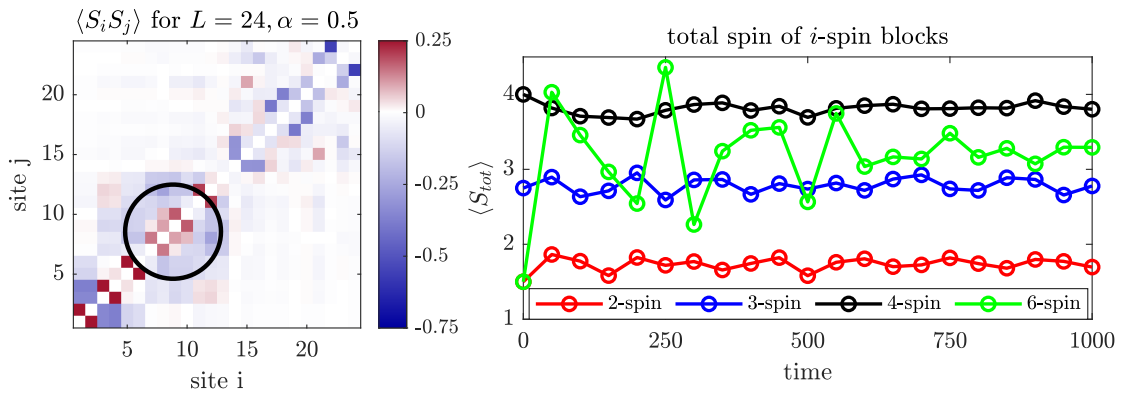


Figure 4.20: Left plot: $\langle S_i S_j \rangle$ color-plot of the final state ($t = 1000$) of a disordered configuration of size $L = 24$. Right plot: time evolution of the total spin \mathbf{S}_{tot} of blocks of 2, 3, 4 and 6 spins in the circled region

The total spin of an i -spin block is:

$$\langle \mathbf{S}_{tot}^2 \rangle = \left(\sum_j \mathbf{S}_j^2 \right)^2 \quad (4.8)$$

The terms $\langle S_i S_j \rangle$ needed for the above calculation are all known from the calculation of the spin-spin correlation matrix. In Fig.4.20 and Fig.4.21 the time evolution of the total spin of i -spin blocks is presented.

The time evolution of the total spin presented above indicates that the sub-thermal regime supports spin-blocks of different sizes, which can be characterized by (quasi-)local integrals of motion, like the total spin, that are conserved over time. The existence of these localized spin-blocks that break the ergodicity of the systems, leads

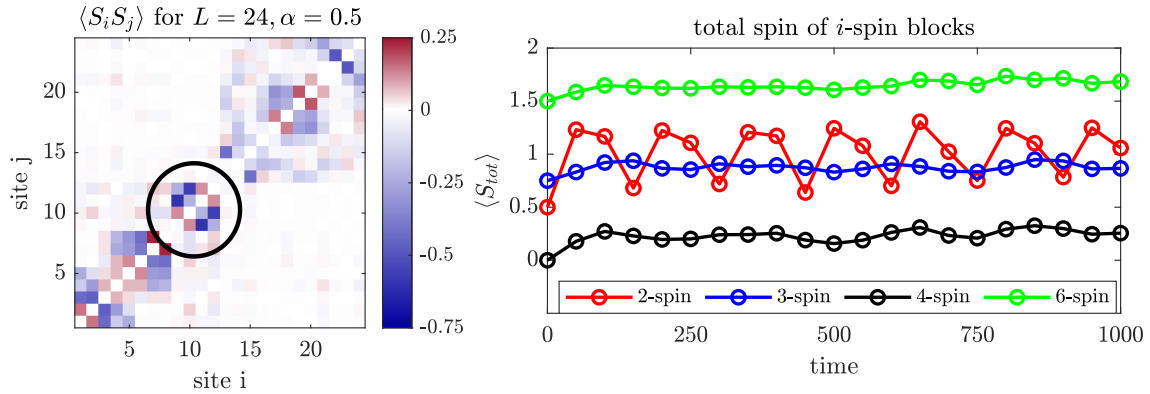


Figure 4.21: Left plot: $\langle S_i S_j \rangle$ color-plot of the final state ($t = 1000$) of a disordered configuration of size $L = 24$. Right plot: time evolution of the total spin \mathbf{S}_{tot} of blocks of 2, 3, 4 and 6 spins in the circled region

to the results shown in previous sections. The above observation is in agreement with the description of the sub-thermal regime using integrals of motion of varying locality.

Chapter 5

Summary and Discussion

In the current master thesis we study how continuous non-Abelian symmetries affect the tendency of a system towards the Many-body localization phase or thermalization. In particular, we study the $SU(2)$ and $SU(3)$ disordered Heisenberg model, where the disorder is added to the model by random coupling constants. We approach the problem through time evolution by implementing a powerful tdDMRG algorithm based on the QSpace tensor network library.

The first step we had to take was the construction of a suitable initial state for each symmetry case. This step is quite important, because it determines the total energy of the system throughout the whole time evolution process, as total energy remains constant. For the study of ETH or/and MBL the energy of the states studied are chosen to be close to the middle of the spectrum, where the density of states is significantly large. With that idea in mind, we choose the symmetry subspaces of the initial chain in such a way that will guarantee a high-energy initialization, as described in chapter 3.

The choice of the disorder strength follows a recent work [1] on the $SU(2)$ Heisenberg model. We choose two disorder strength regimes, one of strong disorder ($\alpha = 0.5$) and one of weaker disorder strength ($\alpha = 1$). For each case of disorder, we generate random J-coupling configurations, drawn from a beta power law distribution. As we are also interested in a system size analysis, we work with 3 cases of chain lengths, $L = \{24, 48, 96\}$. Thus, the parameters of the problem are the disorder strength, system size and symmetry.

Next, we implement the time evolution algorithm for a time interval $t = 1000$, time step $\delta\tau = 0.1$ and bond dimension equal to 1024. For each 3-parameter combination, we produce ~ 20 time evolved states. Then, it is finally the time to start the analysis of the results.

Our analysis is based on two quantities: the spin-spin correlations and the entanglement entropy scaling with length, as described in chapter 4. Starting with the $SU(2)$ symmetric model, for small chains ($L = 24$), we observe the breaking of ergodicity for strong disorder and an ergodic behavior for weaker disorder. These results confirm the ED results produced in a previous study [1] for $L = 22$ sites chains. Extending our analysis to larger chains, we see evidence of the systems tendency towards ergodicity even in the strong disorder regime. Further study is necessary on that ergodic/non-ergodic border. In particular, we plan to make the entropy scaling

analysis for large chains ($L = 96$) a bit more straightforward to ensure the tendency towards thermalization very soon after the end of this master project.

As mentioned above, we could also attack the $SU(3)$ symmetric problem, by making use of the powerful QSpace tensor network library. Using the same random J-configurations, we show evidence of the disappearance of the ergodicity breaking, observed for small chains and strong disorder in the $SU(2)$ case. In other words, even small chains under strong disorder tend to move towards the thermal phase, something that was prohibited by the $SU(2)$ symmetry.

Finally, we tried to understand some of the dynamics concerning the non-ergodic regime observed. For that we studied the total spin and block entropy of localized blocks of different sizes that remain localized in time. We observed, that in the subthermal regime, localized blocks, of varying sizes, are formed, characterized by constant total spin. This comes in agreement with the assumption that the subthermal regime is characterized by integrals of motion of varying locality.

Of course, there are some points that remain unclear or need further analysis. Firstly, a more careful analysis of the entanglement entropy scaling is needed, so that we make our claims more solid. In particular, the next step planned is to produce a larger number of realizations for all the cases studied and improve the entropy scaling results. Moreover, it would be interesting to check if even stronger disorder could extend the non-ergodic behavior to even larger chains, or maybe to the $SU(3)$ symmetric model. Finally, an infinite size analysis of the problem may be a topic of interest.

Appendices

Appendix A

Tensor networks

A.1 Notation

An n -th rank tensor, that lives in an m -dimensional space, is a mathematical object that contains m^n components and obeys certain transformation rules. It can be seen as a generalization of a vector or matrix, and in our case as an array of complex or real numbers. Graphically, we will represent tensors as circles with n legs, where n is the dimension of the tensor. We will note the upper indices (M^i) with an arrow going inwards and the lower indices (M_i) with one going outwards.

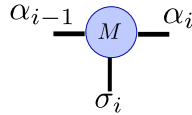


Figure A.1: Illustration of a tensor

A.2 Matrix Product States (MPS)

Throughout this thesis, we will work with one-dimensional disordered Heisenberg spin chains. In Tensor Networks' language, we can represent one dimensional quantum states via Matrix-product states (MPS). Let us consider a general quantum chain $|\psi\rangle$, which can be written as:

$$|\psi\rangle = \sum_{\sigma_1, \dots, \sigma_N} c^{\sigma_1, \dots, \sigma_N} |\sigma_1, \dots, \sigma_N\rangle \quad (\text{A.1})$$

We can think of the coefficient $c^{\sigma_1, \dots, \sigma_N}$ as a tensor with N indices. This tensor can be written as the product of N rank-3 tensors, as follows:

$$|\psi\rangle = \sum_{\sigma_1, \dots, \sigma_N} M_{1;\alpha_1}^{\sigma_1} M_{2;\alpha_2}^{\alpha_1 \sigma_2} \dots M_{N;\alpha_N}^{\alpha_{N-1} \sigma_N} |\sigma_1\rangle \otimes \dots \otimes |\sigma_N\rangle \quad (\text{A.2})$$

That way, we can describe our state ψ as a matrix product. The σ_i indices are the ‘physical’ indices, containing the information of the local physical states on site i , while the α_i indices are the virtual bond ones.

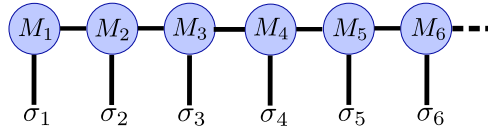


Figure A.2: Illustration of an MPS

A.3 Matrix Product Operators (MPO)

In a similar way, we can represent any operator as a contraction of tensors. An arbitrary operator \hat{O} acting on N sites can be written in the following general form:

$$\hat{O} = |\vec{\sigma}'\rangle O_{\vec{\sigma}}^{\vec{\sigma}'} \langle \vec{\sigma}| = \sum_{\substack{\sigma_1, \dots, \sigma_N \\ \sigma'_1, \dots, \sigma'_N}} c_{\sigma_1, \dots, \sigma_N}^{\sigma'_1, \dots, \sigma'_N} |\sigma_1, \dots, \sigma_N\rangle \langle \sigma'_1, \dots, \sigma'_N| \quad (\text{A.3})$$

Analogously to the MPS construction, we can write the $c_{\sigma_1, \dots, \sigma_N}^{\sigma'_1, \dots, \sigma'_N}$ as a product of N rank-4 tensors, as:

$$\hat{O} = \sum_{\substack{\sigma_1, \dots, \sigma_N \\ \sigma'_1, \dots, \sigma'_N \\ \alpha_1, \dots, \alpha_N}} O_{1;\sigma_1, \alpha_1}^{\sigma'_1} O_{2;\sigma_2, \alpha_1, \alpha_2}^{\sigma'_2} \dots O_{N;\sigma_N, \alpha_{N-1}, \alpha_N}^{\sigma'_N} |\sigma_1, \dots, \sigma_N\rangle \langle \sigma'_1, \dots, \sigma'_N| \quad (\text{A.4})$$

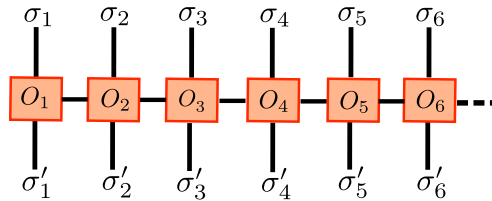


Figure A.3: Illustration of MPO

A.4 Singular Value Decomposition (SVD)

Singular Value Decomposition (SVD) is a quite useful linear algebra tool, which is used in various cases and operations that involve manipulation of MPSs. In fact, the Schmidt decomposition of quantum states can be derived from the Singular Value Decomposition.

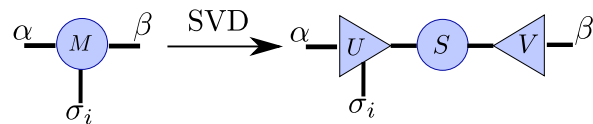


Figure A.4: Singular value decomposition in the tensor networks representation

SVD implies that any matrix M with dimensions $N_A \times N_B$ can be decomposed as:

$$M = USV^\dagger \quad (\text{A.5})$$

U is a $N_A \times \min(N_A, N_B)$ matrix, while V^\dagger is of dimension $\min(N_A, N_B) \times N_B$. U has orthonormal columns, while V^\dagger orthonormal rows. This means that if $N_A \leq N_B$ then U is unitary ($UU^\dagger = I$). Instead, if $N_A > N_B$ then V^\dagger is unitary ($VV^\dagger = I$). S is a diagonal $\min(N_A, N_B) \times \min(N_A, N_B)$ matrix with non-negative elements, called singular values. The number of the non-zero elements is the Schmidt rank of M .

Most of tensor network methods, like DMRG/tDMRG that we will use, rely on the optimal approximation of large dimensional matrices via truncation. Such a truncation can be applied on the S matrix. In particular, for a matrix S with r singular values, written in a descending order, we can set the last $r - r'$ to be zero. This will also lead to a U and V^\dagger matrix of smaller size, and eventually to a matrix M' of rank r' , as an approximation of the initial M .

A.5 Density Matrix Renormalization Group (DMRG)

One dimensional strongly correlated quantum systems are very hard to tackle, both analytically and numerically. There is a variety of approaches, such as the Bethe ansatz, perturbation theory or field theories, but they all encounter restrictions or difficulties to implement. The density-matrix renormalization group (DMRG), invented by White in 1992 [56–60], seems to be one of the most powerful numerical approaches we have in our hands to tackle such one-dimensional problems [48]. It is excessively used for studies on ground state problems, dynamic properties of eigenstates, one-dimensional quantum systems at finite temperature as well as far from equilibrium systems described by non-Hermitian Hamiltonians.

Algorithm

Given a Hamiltonian \hat{H} , DMRG offers a variational method to search for the ground state and ground state energy of \hat{H} . It is based on the assumption, valid for 1-d, which states that we can decimate the Hilbert space of the problem and find a reduced state space that contains all the relevant physics.

In the tensor network language, we consider an MPS of bond dimension D , which will be the dimension of the reduced state space. The first goal is to minimize $\langle \psi | \hat{H} | \psi \rangle$ in the D -dimensional variational space, where $|\psi\rangle$ is represented by the MPS and the Hamiltonian is in an MPO form. Introducing a Lagrange multiplier λ , the goal is the minimization of:

$$\langle \psi | \hat{H} | \psi \rangle - \lambda \langle \psi | \psi \rangle \quad (\text{A.6})$$

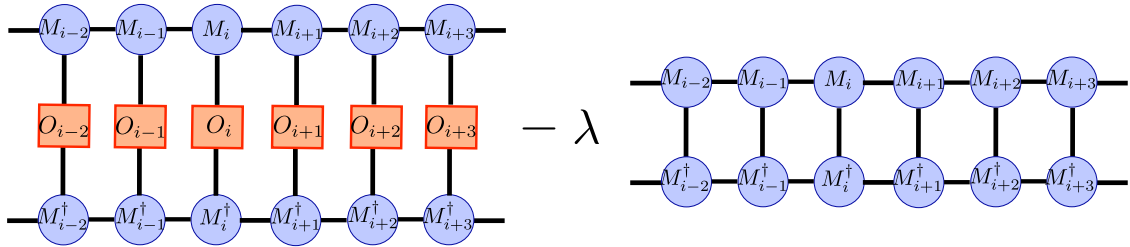


Figure A.5: $\langle \psi | \hat{H} | \psi \rangle - \lambda \langle \psi | \psi \rangle$ in tensor networks' representation

The next step is to extremize the above quantity with respect to an MPS tensor. This is part of the one-site formulation of DMRG. However, the one-site procedure is not suitable for problems that involve symmetries, as an one-site update is limited to the Hilbert space of its symmetry sector. Instead, a two-site formulation of DMRG is used and we will describe the following steps of it below.

- Firstly, we prepare our MPS in a mixed canonical form around one of the two tensors (M_i, M_{i+1}), with respect to which we want to extremize Eq.A.6.

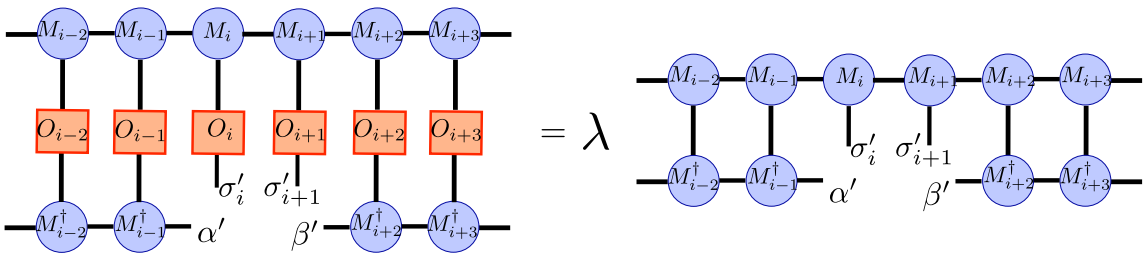


Figure A.6: Minimization of $\langle \psi | \hat{H} | \psi \rangle - \lambda \langle \psi | \psi \rangle$

- The updated pair of M_i, M_{i+1} is given by extremizing Eq.A.6 with respect to $M_i^\dagger, M_{i+1}^\dagger$

$$\frac{\partial}{\partial M_{i+1}^\dagger} \frac{\partial}{\partial M_i^\dagger} \left(\langle \psi | \hat{H} | \psi \rangle - \lambda \langle \psi | | \psi \rangle \right) \stackrel{!}{=} 0 \quad (\text{A.7})$$

The derivation above leads to a generalized eigenvalue problem written in tensor format as:

$$H_\alpha^{\alpha'} (M_i M_{i+1})^\alpha = \lambda (M_i M_{i+1})^{\alpha'} \quad (\text{A.8})$$

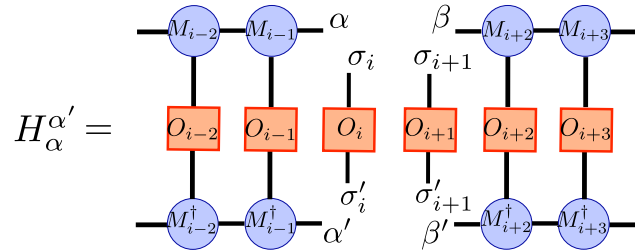


Figure A.7: $H_\alpha^{\alpha'}$ in tensor networks' representation

- The following step is to solve the eigenvalue problem above, and in particular find the lowest eigenvalue. For that the Lanczos iterative algorithm is used [61–64], as the size of the update is $Dd \times Dd$.
- Last step of the optimization is the reshape of the updated tensors $\tilde{M}_i \tilde{M}_{i+1}$ and truncation down to size D .

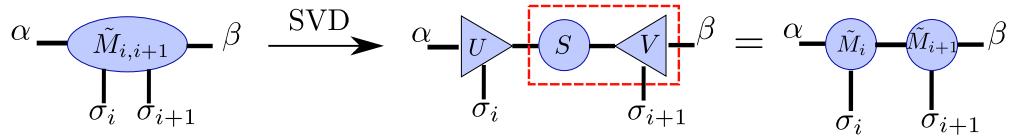


Figure A.8: Final step of the $\tilde{M}_i \tilde{M}_{i+1}$ tensors update

- The above steps complete the optimization of the pair $M_i M_{i+1}$. Then, we move to the next pair $M_{i+1} M_{i+2}$ to the write and repeat the steps above. The algorithm repeats sweeps to the right and left through the whole MPS till there is convergence

Bibliography

- [1] I.V. Protopopov, R.K. Panda, T. Parolini, A. Scardicchio, E. Demler, and D.A. Abanin. “Non-Abelian symmetries and disorder: A broad nonergodic regime and anomalous thermalization”. In: *Phys. Rev. X* 10 011025 (2020).
- [2] Rigol M., Dunjko V., and Olshanii M. “Thermalization and its mechanism for generic isolated quantum systems”. In: *Nature* 452 (2008), pp. 854–858.
- [3] J. M. Deutsch. “Quantum statistical mechanics in a closed system”. In: *Phys. Rev. A* 43, 2046-2049 (1991).
- [4] Mark Srednicki. “Chaos and quantum thermalization”. In: *Phys. Rev. E* 50, 888-901 (1994).
- [5] D’Alessio Luca, Yariv Kafri, Anatoli Polkovnikov, and Marcos Rigol. “From quantum chaos and eigenstate thermalization to statistical mechanics and thermodynamics”. In: *Advances in Physics* 65 (3), 239-362 (2016).
- [6] Nandkishore Rahul and David A. Huse. “Many-body localization and thermalization in quantum statistical mechanics”. In: *Annual Review of Condensed Matter Physics* 6 (1), 15-38 (2015).
- [7] Mark Srednicki. “The approach to thermal equilibrium in quantized chaotic systems”. In: *Journal of Physics A: Mathematical and General* 32 (7), 1163 (1999).
- [8] P.W. Anderson. “Absence of diffusion in certain random lattices”. In: *Phys. Rev.* 109 (1958), p. 1492.
- [9] S.A. Parameswaran, A.C. Potter, and R. Vasseur. “Recent progress in many-body localization”. In: *Annalen der Physik* (2017), p. 1700169.
- [10] D.A. Abanin, E. Altman, I. Bloch, and M. Serbyn. “Colloquium: Many-body localization, thermalization and entanglement”. In: *Rev. Mod. Phys* 91 (2019), p. 021001.
- [11] F. Alet and N. Laflorencie. “Many-body localization: An introduction and selected topics”. In: *Comptes Rendus Physique* 19.6 (2018), pp. 498–525.
- [12] S.A. Parameswaran, A.C. Potter, and R. Vasseur. “Eigenstate phase transitions and the emergence of universal dynamics in highly excited states”. In: *Annalen der Physik* (2017), p. 1600302.
- [13] A. Pal and D.A. Huse. “Many-body localization phase transition”. In: *Phys. Rev. B* 82 (2010), p. 174411.

- [14] R. Singh, J.H. Bardarson, and F. Pollmann. “Signatures of the many-body localization transition in the dynamics of the entanglement and bipartite fluctuations”. In: *New J. Phys* 18 (2016), p. 023046.
- [15] A.C. Potter, R. Vasseur, and S.A. Parameswaran. “Universal properties of many-body delocalization transitions”. In: *Phys. Rev. X* 5 (2015), p. 031033.
- [16] R. Vosk, D.A. Huse, and E. Altman. “Theory of the many-body localization transition in one-dimensional systems”. In: *Phys. Rev. X* 5 (2015), p. 031032.
- [17] P.D.J. Luitz, N. Laflorencie, and F. Alet. “Many-body localization edge in the random-field Heisenberg chain”. In: *Phys. Rev. B* 91 (2015), p. 081103.
- [18] S.P. Lim and D.N. Sheng. “Many-body localization and transition by density matrix renormalization group and exact diagonalization studies”. In: *Phys. Rev. B* 94 (2016), p. 045111.
- [19] T. Devakul and R.R.P. Singh. “Early breakdown of area law entanglement at the many-body delocalization transition”. In: *Phys. Rev. Lett* 115 (2015), p. 187201.
- [20] A. Pal and David A. Huse. “Many-body localization phase transition”. In: *Phys. Rev. B* 82 174411 (2010).
- [21] M. Rigol. “Breakdown of thermalization in finite one-dimensional systems”. In: *Phys. Rev. Lett* 103 (2009), p. 100403.
- [22] D.J. Luitz. “Long tail distributions near the many-body localization transition”. In: *Phys. Rev. B* 93 (2016), p. 134201.
- [23] P. Sierant, D. Delande, and J. Zakrzewski. “Many-body localization due to random interactions”. In: *Phys. Rev. A* 95 (2017), p. 021601.
- [24] Y.B. Lev, D.R. Reichman, and Y. Sagi. “Many-body localization in system with a completely delocalized single-particle spectrum”. In: *Phys. Rev. B* 94 (2016), p. 201116.
- [25] V. Oganesyan and David A. Huse. “Localization of interacting fermions at high temperature”. In: *Phys. Rev. B* 75 155111 (2007).
- [26] P. Prelovsek, M. Mierzejewski, O. Barisic, and J. Herbrych. “Density correlations and transport in models of many-body localization”. In: *Annalen der Physik* 529 (2017), p. 1600350.
- [27] D.J. Luitz and Y.B. Lev. “The ergodic side of the many-body localization transition”. In: *Annalen der Physik* 529 (2017).
- [28] J.A. Kjäll, J.H. Bardarson, and F. Pollmann. “Many-body localization in a disordered quantum Ising chain”. In: *Phys. Rev. Lett.* 113 (2014), p. 107204.
- [29] E. Baygan, S.P. Lim, and D.N. Sheng. “Many-body localization and mobility edge in a disordered spin-1/2 Heisenberg ladder”. In: *Phys. Rev. B* 92 (2015), p. 195153.
- [30] C.R. Laumann, A. Pal, and A. Scardicchio. “Many-body mobility edge in a mean-field quantum spin glass”. In: *Phys. Rev. Lett* 113 (2014), p. 200405.

- [31] I. Mondragon-Shem, A. Pal, T.L. Hughes, and C.R. Laumann. “Many-body mobility edge due to symmetry-constrained dynamics and strong interactions”. In: *Phys. Rev. B* 92 (2015), p. 064203.
- [32] B. Villalonga, X. Yu, D.J. Luitz, and B.K. Clark. “Exploring one-particle orbitals in large many-body localized systems”. In: *Phys. Rev. B* 97 (2018), p. 104406.
- [33] W. De Roeck, F. Huveneers, M. Müller, and M. Schiulaz. “Absence of many-body mobility edges”. In: *Phys. Rev. B* 93 (2016), p. 014203.
- [34] M. Ovadia, D. Kalok, I. Tamir, S. Mitra, B. Sacépé, and D. Shahar. “Evidence for a finite-temperature insulator”. In: *Scientific Reports* 5 (2015), p. 13503.
- [35] M. Schreiber, S.S. Hodgman, P. Bordia, H.P. Lüschen, M.H. Fischer, R. Vosk, E. Altman, U. Schneider, and I. Bloch. “Observation of many-body localization of interacting fermions in a quasirandom optical lattice”. In: *Science* 349 (2015), pp. 842–845.
- [36] J. Choi, S. Hild, J. Zeiher, P. Schauss, A. Rubio-Abadal, T. Yefsah, Vedika Khemani, D.A. Huse, I. Bloch, and C. Gross. “Exploring the many-body localization transition in two dimensions”. In: *Science* 352 (2016), pp. 1547–1552.
- [37] J. Smith, A. Lee, P. Richerme, B. Neyenhuis, P.W. Hess, P. Hauke, M. Heyl, D.A. Huse, and C. Monroe. “Many-body localization in a quantum simulator with programmable random disorder”. In: *Nature Physics* 12 (2016), pp. 907–911.
- [38] P. Roushan *et al.* “Spectroscopic signatures of localization with interacting photons in superconducting qubits”. In: *Science* 1175-1179 (2017), p. 358.
- [39] A. A. Houck, H.E. Türeci, and J. Koch. “On-chip quantum simulation with superconducting circuits”. In: *Nature Physics* 8 (2012), pp. 292–299.
- [40] K. Xu, J. Chen, Y. Zeng, Y. Zhang, C. Song, W. Liu, Q. Guo, P. Zhang, D. Xu, H. Deng, K. Huang, H. Wang, X. Zhu, D. Zheng, and H. Fan. “Emulating many-body localization with a superconducting quantum processor”. In: *Phys. Rev. Lett.* 120 (2018), p. 050507.
- [41] A.C. Potter and R. Vasseur. “Symmetry constraints on many-body localization”. In: *Phys. Rev. B* 94 (2016), p. 224206.
- [42] R. Vasseur, A.J. Friedman, S.A. Parameswaran, and A.C. Potter. “Particle-hole symmetry, many-body localization and topological edge modes”. In: *Phys. Rev. B* 93 (2016), p. 134207.
- [43] R. Vasseur, A.C. Potter, and S.A. Parameswaran. “Quantum criticality of hot random spin chains”. In: *Phys. Rev. Lett.* 114 (2015), p. 217201.
- [44] I.V. Protopopov, W.W. Ho, and D.A. Abanin. “The effect of $SU(2)$ symmetry on many-body localization and thermalization”. In: *Phys. Rev. B* 96 041122 (2017).
- [45] C. Dasgupta and S. Ma. “Low-temperature properties of the random of the random Heisenberg antiferromagnetic chain”. In: *Phys. Rev. B* 22 (1980).

- [46] S. Ma, C. Dasgupta, and C. Hu. “Random antiferromagnetic chain”. In: *Phys. Rev. Lett.* 43 (1979), p. 1434.
- [47] J.C. Scott, A.F. Garito, A. J. Heeger, P. Nannelli, and H.D. Gillman. “Magnetic properties of Poly(Metal Phosphinates): The effects of structural disorder on one-dimensional antiferromagnetic chains”. In: *Phys. Rev. B* 12 (1975), p. 356.
- [48] U. Schollwöck. “The density-matrix renormalization group in the age of matrix product states”. In: *Annals of Physics* 326 96-192 (2011).
- [49] S. Paeckel, T. Köhler, A. Swoboda, S. R. Manmana, U. Schollwöck, and C. Hübiger. “Time-evolution methods for matrix-product states”. In: *Annals of Physics* 411 167998 (2019).
- [50] A. Weichselbaum. “Non-abelian symmetries in tensor networks: A quantum symmetry space approach”. In: *Annals of Physics* 327.12 (2012), pp. 2972–3047.
- [51] A. J. Daley, C. Kollath, U. Schollwöck, and G. Vidal. “Time-dependent density-matrix renormalization-group using adaptive effective Hilbert spaces”. In: *J. Stat. Mech* P04005 (2004).
- [52] S.R. White and A.E. Feiguin. “Real-time evolution using the Density Matrix Renormalization Group”. In: *Phys. Rev. Lett.* 93 076401 (2014).
- [53] T. Lezama, S. Bera, H. Schomerus, F. Heidrich-Meisner, and J. H. Bardarson. “One-particle-density-matrix occupation spectrum of many-body localized states after a global quench”. In: *Phys. Rev. B* 96 060202(R) (2017).
- [54] X. Yu, D.J. Luitz, and B.K. Clark. “Bimodal entanglement entropy distribution in many-body localization transition”. In: *Phys. Rev. B* 94 184202 (2016).
- [55] A. Prakash, S. Ganeshan, L. Fidkowski, and T.C. Wei. “Eigenstate phases with finite on-site non-Abelian symmetry”. In: *Phys. Rev. B* 96 165136 (2017).
- [56] Steven R. White. “Density matrix formulation for quantum renormalization groups”. In: *Phys. Rev. Lett.* 69.19 (1992), pp. 2863–2866.
- [57] Steven R. White. “Density-matrix algorithms for quantum renormalization groups”. In: *Phys. Rev. B* 48 (1993), p. 10345.
- [58] G. Vidal. In: *Phys. Rev. Lett.* 91 (2003), p. 147902.
- [59] Guifré Vidal. “Efficient Simulation of One-Dimensional Quantum Many-Body Systems”. In: *Phys. Rev. Lett.* 93.4 (2004), p. 040502.
- [60] F. Verstraete, J.J. Garcia-Ripoll, and J.I. Cirac. “Matrix Product Density Operators: Simulation of Finite-Temperature and Dissipative Systems”. In: *Phys. Rev. Lett.* 93 (2004), p. 207204.
- [61] C. Lanczos. “An iteration method for the solution of the eigenvalue problem of linear differential and integral operators”. In: *J. Res. Nat’l. Bur. Std.* 45 (1950), pp. 255–282.
- [62] Ojalvo I.U. and Newman M. J. “Vibration modes of large structures by an automatic matrix-reduction method”. In: *AIAA J.* 8 (1970), pp. 1234–1239.

- [63] Paige C.C. “Computational variants of the Lanczos method for the eigenproblem”. In: *J. Inst. Maths Applics* 10 (1972), pp. 373–381.
- [64] Erik Koch. *The Lanczos Method*. Ed. by Eva Pavarini, Erik Koch, Dieter Vollhardt, and Alexander Lichtenstein. 2011.

Declaration

I hereby declare that this thesis is my own work, and that I have not used any sources and aids other than those stated in the thesis.

München, 28.02.2022

A handwritten signature in black ink, appearing to read 'Dimitris Saraidaris', written in a cursive style.

Dimitris Saraidaris

